CALIFORNIA INSTITUTE OF TECHNOLOGY
Physics, Mathematics and Astrophysics Division

DESIGN AND SIMULATION OF A LIGHT-WEIGHT TELESCOPE MOUNT FOR THE BICEP ARRAY RECEIVER BEAM CHARACTERIZATION

ASI-CAIF Summer Internship final report

SUPERVISORS
Prof. James J. Bock
Dr. Lorenzo Moncelsi
Dr. Alessandro Schillaci

INTERN
Paolo Gennaro Madonia

July - September 2018

ABSTRACT

During this summer internship program funded by the *Italian Space Agency (ASI)* and the *Cultural Association of Italians at Fermilab (CAIF)*, I worked within Caltech's Observational Cosmology group on the *BICEP Array* project.

BICEP Array will study the very early Universe through measurements of the Cosmic Microwave Background polarization from the South Pole. The aim of my internship was to retrofit a pre-existing alt-azimuthal mount located in the Caltech High Bay – known as *"AzEl mount"* - for testing operations of the BICEP Array receivers. The project involved the design and structural simulations of a support part needed to attach the telescope's cryostat onto the AzEl mount. During this period I also took part in the integration of BICEP Array receiver and in the operations for its first cryogenic run performed at Caltech, for which I designed a dedicated warm junction box for the housekeeping system of the instrument.

In Chapter 1 I briefly introduce the scientific goal of BICEP Array and provide a general description of the instrument; in Chapter 2 I present the design and simulation work related to the retrofit of the AzEl mount; in Chapter 3 I present the making of the warm housekeeping box for the instrument tests at Caltech; finally, in Appendix A I have put additional figures from the simulations, while in Appendix B a test on possible leaks inside the cryostat is presented.

CONTENTS

1 BICEP ARRAY: SCIENCE AND INSTRUMENT DESCRIPTION

BICEP Array [Hui et al., 2018] is the fourth generation experiment of the *BICEP/Keck Array program*, which will start its operation at the South Pole during the 2019-2020 season: this experiment is the result of the huge experimental effort that cosmologists have put in the last two decades in searching the *polarization B-modes* of the Cosmic Microwave Background (CMB). Measuring the polarization features of the CMB can indeed provide critical information on the primordial phases of our Universe, in particular on the *inflationary era*: the inflationary theory [Guth, 1981] predicts that soon after the Big Bang the Universe experienced a phase of accelerated (almost exponential) expansion during a really short period of time. This theory has not been proved directly yet, but it provides a satisfactory solution to the problems of the standard Big Bang model, and up to now it has never been in conflict with the observations.

One of the features expected to be produced during the inflation is a stochastic background of *primordial gravitational waves* (see Kamionkowski and Kovetz [2016] and references therein): these tensor perturbations are expected to induce a gradient-free *B-mode* in the polarization of the CMB, opposed to a curl-free polarization *E-mode* expected to be induced by both scalar (e.g. density) and tensor perturbations; an example of polarization pattern is given in Figure 1.0.1.

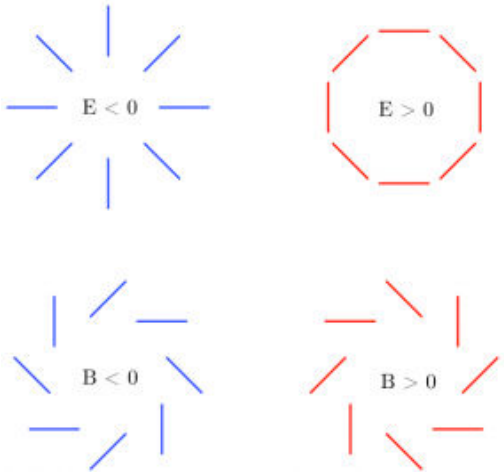

Figure 1.0.1: Examples of two different polarization patterns: the E-mode lines (top) have radial or tangential alignment, the B-mode lines (bottom) are tilted by 45 degrees.

The reason why cosmologist strove to find B-modes in the Cosmic Microwave Background is that although different classes of inflation models could generate undetectably low levels of gravitational waves, a detection of a B-mode pattern generated by primordial gravitational waves would be the *first direct evidence* for the inflationary theory.

In order to separate the really faint CMB signal from the polarized synchrotron and dust foregrounds, BICEP array will need to observe the sky at multiple wavelengths: the instrument is comprised of four separate telescopes which will work at 30/40, 95, 150 and 220/270 GHz with over 30,000 detectors. The design on the instrument [Crumrine et al., 2018] is based on the BICEP3 telescope: the receiver is a 2m tall cryostat hosting two stages that are actively cooled down to 50K and 4K by a pulse tube cryocooler, with a nested sub-K insert cooled by a ^{4}He/^{3}He/^{3}He fridge which will bring the focal plane down to 250mK, the temperature needed to operate

the heart of the instrument, an array of *antenna-coupled Transition Edge Sensors* (TES) bolometers; a section view of the cryostat is shown in Figure 1.0.2.

Before the deployment at South Pole (the 30/40GHz is scheduled to be installed during the 2019-2020 season) the receivers will be characterized, and several tests will be performed: one of the tests that will take place in Caltech's facility will be the *beam calibration* of the 30/40GHz instrument, in order to assess if the optical system behaves in the nominal way before sending the instrument down to the Pole. Beam calibration can be performed in two limits, the *near-field* case and the *far-field*: given a telescope with aperture D operating at a wavelength λ, the limit between these two scenarios is defined by the formula

$$2\frac{D^2}{\lambda}$$

which provides the minimum distance between the source and the telescope in order to be in the far-field approximation (i.e. the wavefronts are plane and parallel). For the BICEP Array 30/40GHz receiver this results[1] in

$$2\frac{D^2}{\lambda} \sim 2\frac{0.56^2}{0.009} \sim 70m$$

so, a large facility is needed for the far-field beam calibration and also a mount large enough to move the cryostat and scan the whole field of view. The main goal of this internship has been to retrofit a mount now located in Caltech's high bay, which in the past was used for tests of the much smaller *SPIDER* telescope.

1 D and λ are expressed in meters.

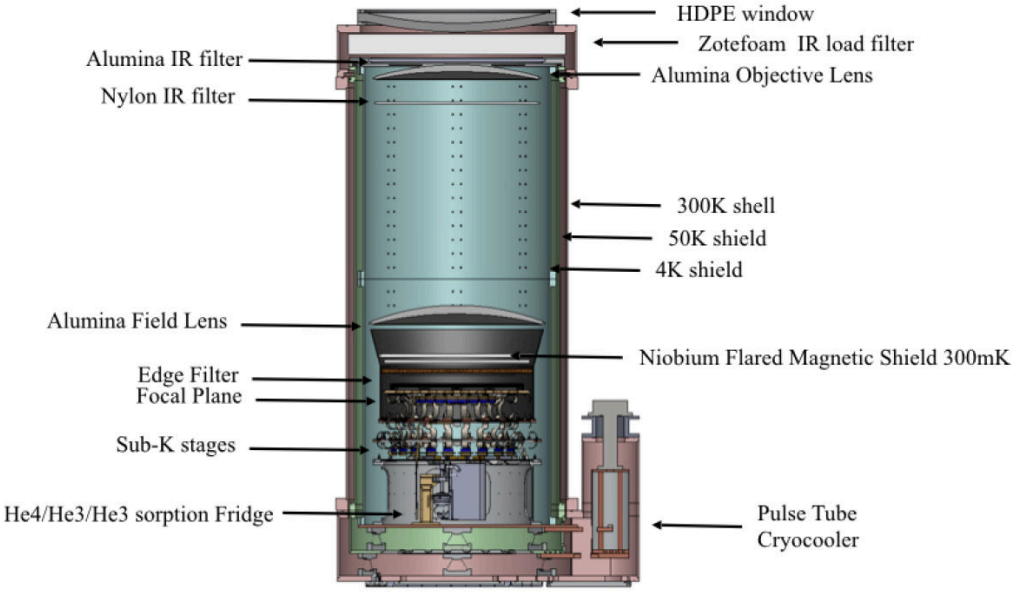

Figure 1.0.2: Section view of one of the BICEP Array receivers. Credit: Hui et al. [2018].

2 THE AZEL MOUNT INTERFACE FOR BICEP ARRAY RECEIVER

In this chapter the design of the mount interface is presented first, while detailed description of the simulations is provided in a following section.

2.1 THE AZEL "GADGET" MOUNT

The *AzEl gadget mount* is an alt-azimuthal scanning platform currently located in Caltech's high bay: it was built by the University of Toronto[1] for the instrument characterization operations of the SPIDER test cryostat; the mount is shown in Figure 2.1.1. The size of this mount is not optimized for the much bigger BICEP Array cryostat, hence the existing support frame has to be replaced with a dedicated interface part for the BA receiver.

2.2 DESIGN OF THE INTERFACE FRAME

The design of the interface was driven by the need of a sufficiently stiff and robust support for the cryostat, which at the same time should be as light as possible and fit inside the existing AzEl mount. The design process

1 The references used for the AzEl gadget specifications and CAD drawings are available at http://galadriel.astro.utoronto.ca/~soler/AzElGadget.html .

Figure 2.1.1: The AzEl Gadget mount.

consisted of three iterations, using the results of the structural simulations to adjust the design from one step to the next one.

2.2.1 First iteration - v0

The first design (see Figure 2.2.1) was used to provide a zero-order estimate on the stability and resistance of the interface frame. This first concept features the following parts:

- *square frame* - made of two identical parts bolted together around the cryostat, this is the element that is directly attached to the mount's trunnions; to provide strength without adding too much weight to the structure, it has been chosen to use aluminum tubes; four plates

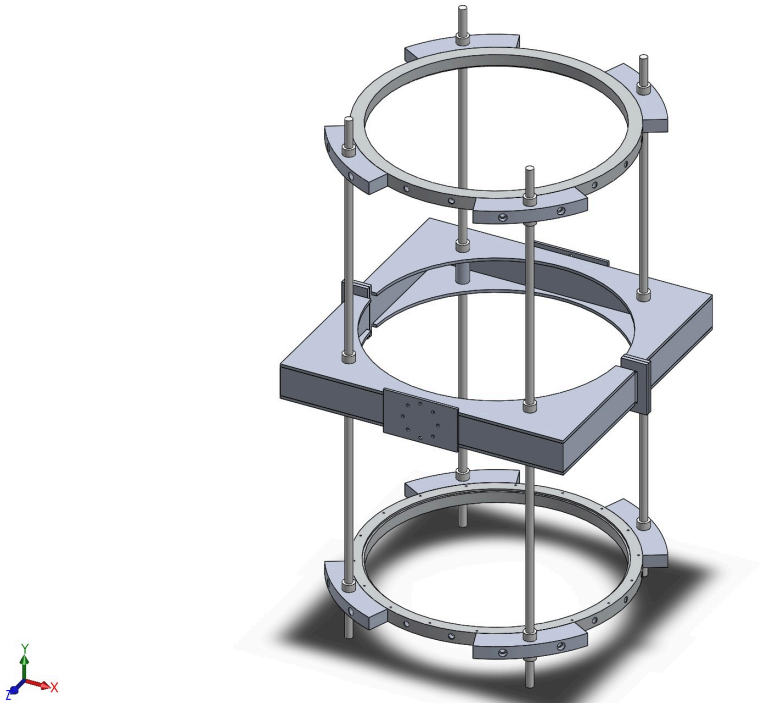

Figure 2.2.1: First design of the cryostat interface support: here is also shown how this structure is connected to the cryostat's upper and lower rings (the rest of the cryostat is hidden).

with a semicircular profile close the top and bottom sides of the frame, following the cryostat profile (a $12.9mm$ gap has been left between the plates and the cryostat's 300K shell)

- *aluminum flanges* - two sets of four aluminum flanges that are attached on the cryostat's upper/lower rings
- *four stainless steel, 1" thick, threaded rods* - these rods pass through the frame and connect it to flanges on the cryostat; they are fixed with stainless steel nuts which allow to move the square frame up and down along the rods for small adjustments

- *four aluminum cylinders* - the purpose of these components is to reduce the stress exerted by the rods on the frame, for which they are placed inside the square frame in correspondence with the holes on the plates.

All the parts are made of *Al 6061-T6*, except for the rods which are made of *ASTM -A354DB stainless steel.*

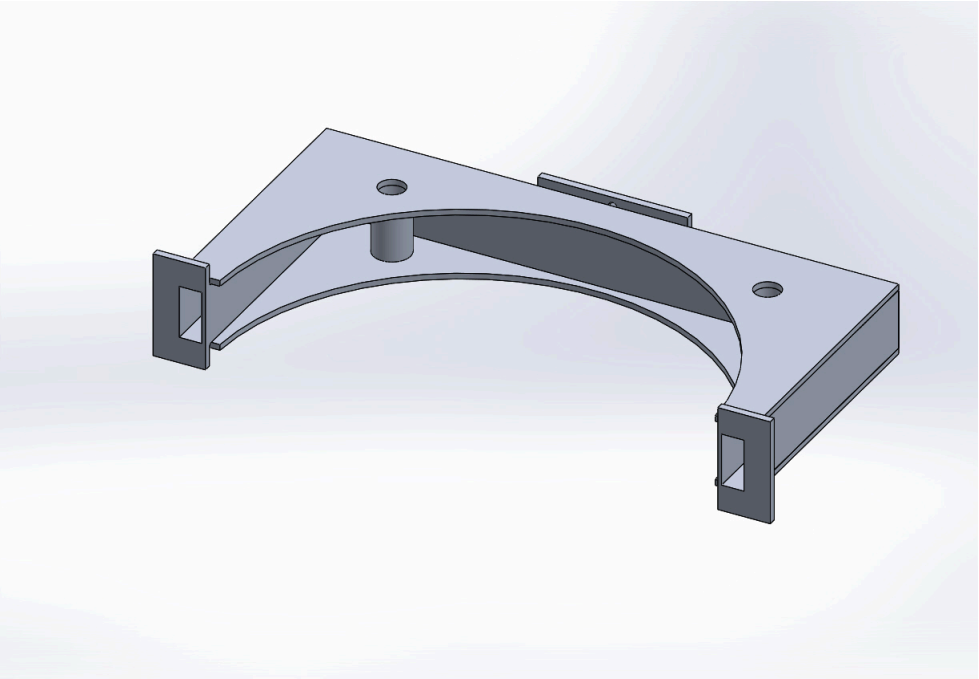

Figure 2.2.2: View of one of the two pieces that make the square frame: one of the cylinders is also visible.

As visible in Figure 2.2.1, in this version the square frame is placed at mid height with respect to the rods: however, this was a preliminary concept used only to investigate the stability of such a kind of structure. Indeed, when the cryostat is placed on the mount, this causes an interference between the *Multi-Channel Electronics (MCE)* box (located at the bottom of the cryostat) and the mount itself. This has been solved in the **v0.1** design,

as showed in Figure 2.2.3: the square frame has been lowered along the rods and an additional aluminum beam has been added on the top of the AzEl mount. Adding the beam is a better solution than moving only the frame by a larger distance, because that would also cause a shift the center of mass much further away from the elevation axis.

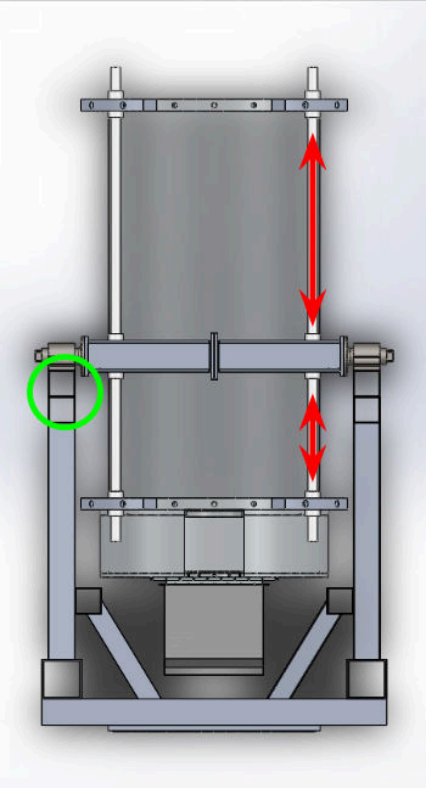

Figure 2.2.3: v0.1 design: here is evident the asymmetric position of the frame with respect to the rods. The combined effect of lowering the frame and adding a new aluminum beam on the mount (highlighted in green) provided enough clearance for the MCE box, visible at the bottom of the cryostat.

2.2.2 Second iteration - v1

The results from the simulation run presented in section 2.3.1 exposed the need for a stronger structure which would be less subject to deformations when the cryostat is tilted, hence this design features $1.5in$ thick rods instead of the $1in$ thick used before. Apart from this modification and from the related ones made on the cylinders and on the plates in order to accommodate for the higher thickness, anything else was changed.

2.2.3 Third iteration - v2

In this version the focus was put on reducing the gap between the *center of mass* (CoM) of the cryostat and the *elevation axis*, as in the previous configuration their separation was larger than $20cm$[2]. At the same time, the position of the center of mass was shifted upwards by the addition of the *Far Field Flat mirror* on the top of the cryostat.

In order to reduce this gap, the square frame was lowered again along the rods, and hence another aluminum tube had to be added to the AzEl mount as happened for v0.1: as shown in Figure 2.2.4 the mount's A-shaped structure would become much taller so, to increase the stability, aluminum plates were added on both sides of the three beams on the top of the fork.

In addition to that, the length of the rods was extended in order to place a few counterweights at the bottom of the cryostat. The resulting final design is shown in Figure 2.2.5.

2 The main component of the separation lies on the cryostat's axis, as its cylindrical symmetry is only broken by the pulse tube assembly located on one side of the receiver.

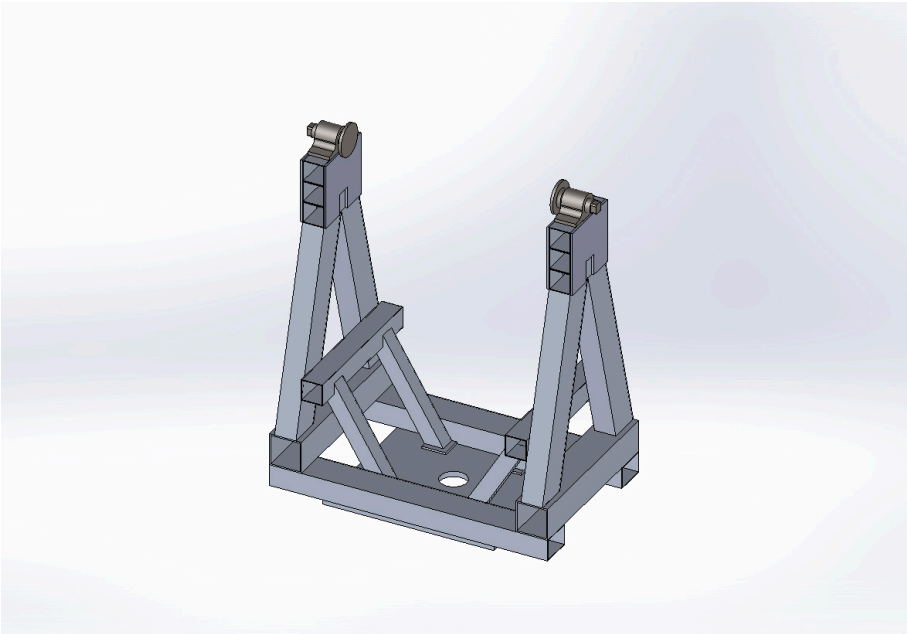

Figure 2.2.4: AzEl mount adapted for the v2 design: two aluminum beams were added to the A-shaped structure, so four aluminum plates were put on both sides of these tubes to increase stability.

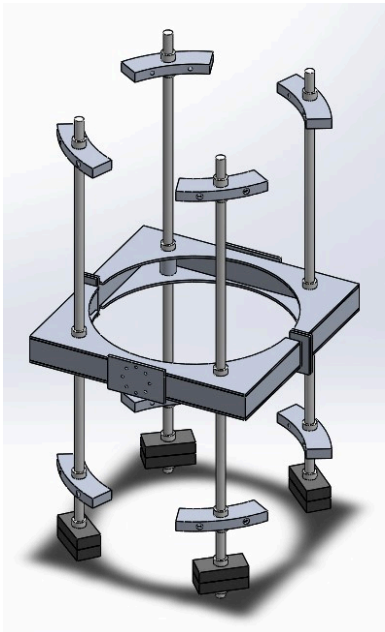

Figure 2.2.5: v2 design: the rods have been extended to add counterweights and the square frame has been lowered along the rods.

2.3 SIMULATIONS OF THE INTERFACE FRAME AND MOUNT

A finite-element static analysis of the structure has been performed using the *SolidWorks Simulation* package. For each configuration, the *Von Mises stress*, the *displacement*, and the *factor of safety*[3] were studied for two scenarios, with the cryostat at $0°$ and $90°$ of inclination from the vertical axis: although the cryostat will never be used in the $90°$ configuration, the structure is required to provide safe support even in the worst case scenario (i.e. with the cryostat horizontal with respect to the floor). In reality, for the beam calibration a *flat folding mirror* will be placed above the receiver (see Section 2.4 for details): the telescope has a $30°$ Field of View (FOV) so, if the source is in its center when the cryostat is in vertical position, the maximum tilt needed to map the whole FOV with some margin will be of $\sim \pm 20°$.

To facilitate the simulation process many parts have been simplified, avoiding to put too many details (e.g. threaded holes, nuts, screws). For the same reason, a dummy cryostat has been used instead of the full cryostat assembly with hundreds of components: only the 300K shield and the two aluminum rings to which the interface frame is attached have been involved in the simulations; moreover, these three parts have been considered rigid. All the connections between parts have been considered as bonded contacts.

3 The factor of safety (FOS) is defined for each point as the tensile strength of the material divided by the stress experienced in that point

In every run, apart from the gravity load, a test load of $1200Kg$ has been applied on the cryostat's external shell: this load is 1.5 times the nominal mass of the cryostat ($\sim 800Kg$).

The physical properties of the materials used in this study are reported in Table 2.3.1.

	Al6061-T6	ASTM-A354DB (SS)
Density (g/cm^3)	2.78	7.85
Tensile strength (MPa)	310	1034
Yield strength (MPa)	276	896

Table 2.3.1: Physical properties of the materials which have been simulated.

2.3.1 v0 simulations

This run involved the interface structure only, so the fixtures were placed on the hinges' plates, as shown in Figure 2.3.1. The results of this run are reported in Table 2.3.2 and in Figures 2.3.2, 2.3.3, 2.3.4 and 2.3.5. The structure resulted safe in the vertical configuration, while it showed quite large deformations in the horizontal configuration (although smaller than the clearance between the cryostat and the square frame). All the stresses were below the tensile strength of the materials.

Inclination (deg)	**0**	**90**
Max Von Mises stress (MPa)	22	62.4
Max displacement (mm)	0.13	1.81
Min factor of safety	13	14

Table 2.3.2: Results of the static analysis of the v0 configuration.

For the v0.1 configuration we were interested in understanding how the deformation changed after breaking the initial planar symmetry, especially

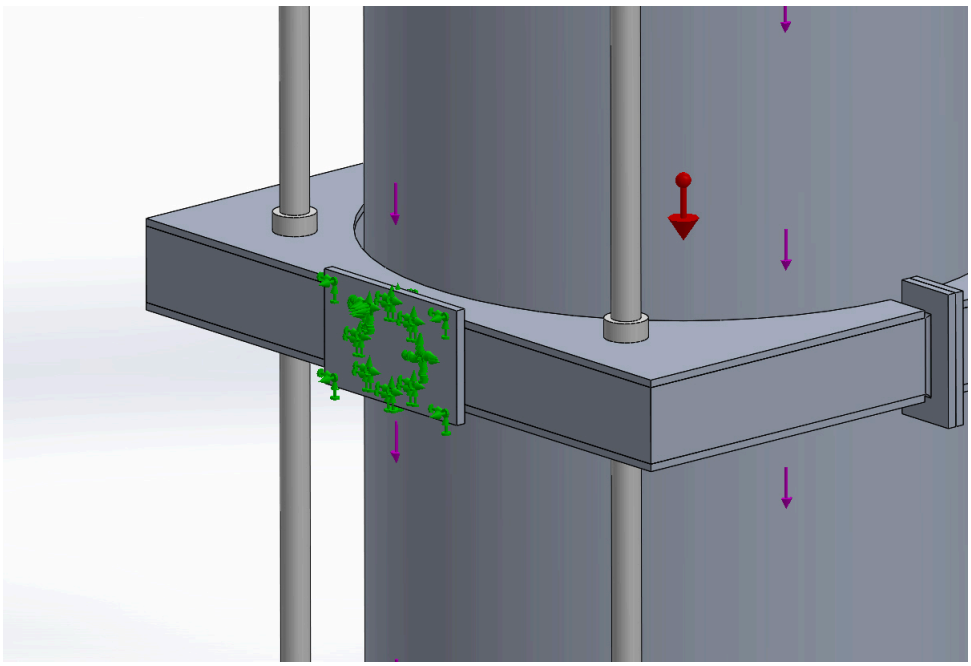

Figure 2.3.1: vo simulations - fixtures and loads are highlighted in different colors: in *green* the fixtures placed on the hinges' plates which connect to the trunnions, in *purple* the test load applied on the cryostat's shell, in *red* the gravity load.

Inclination (deg)	**90**
Max Von Mises stress (MPa)	358.942
Max displacement (mm)	5.99
Min factor of safety	2.5

Table 2.3.3: Results of the static analysis of the vo.1 configuration.

in the 90° configuration: the results are shown in Table 2.3.3. As visible in Figure 2.3.6 **(b)**, shifting the square frame introduced a displacement gradient: although the displacement is once again within the tolerance between the square frame and the cryostat, such a deformation has been considered too high and so the rods were changed with thicker ones.

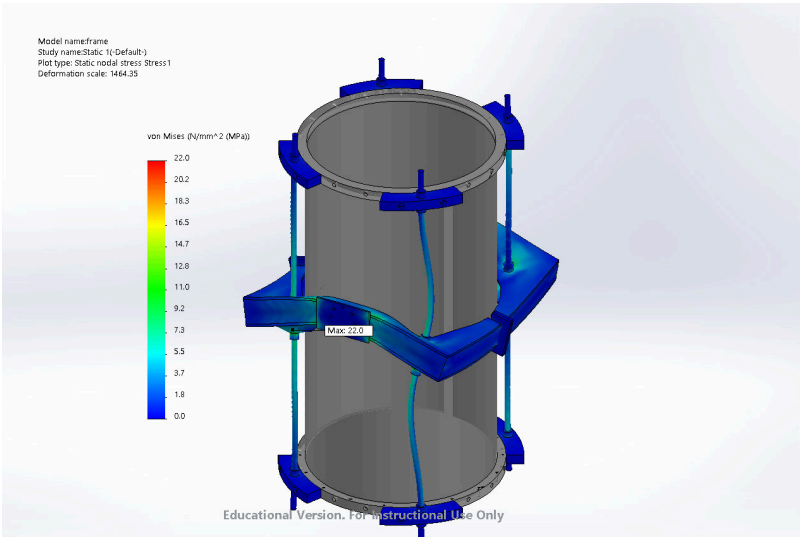

(a)

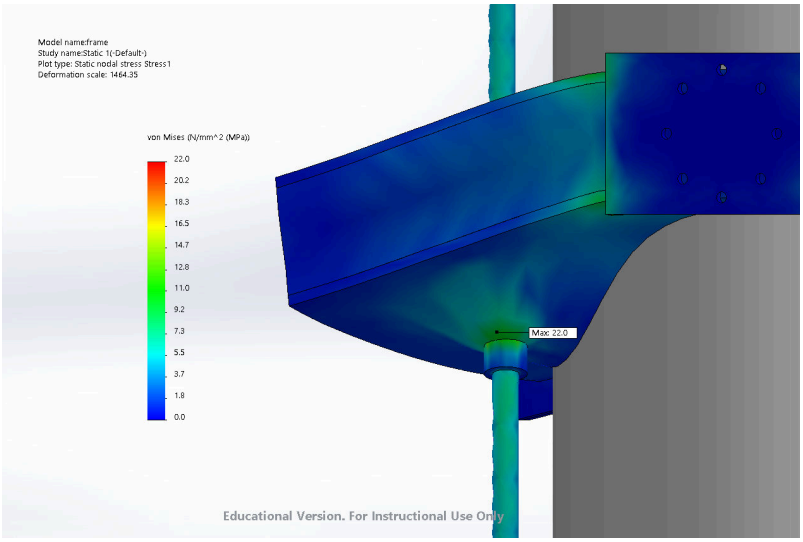

(b)

Figure 2.3.2: Von Mises stress analysis for the v0-0° configuration: complete view **(a)** and particular **(b)**.

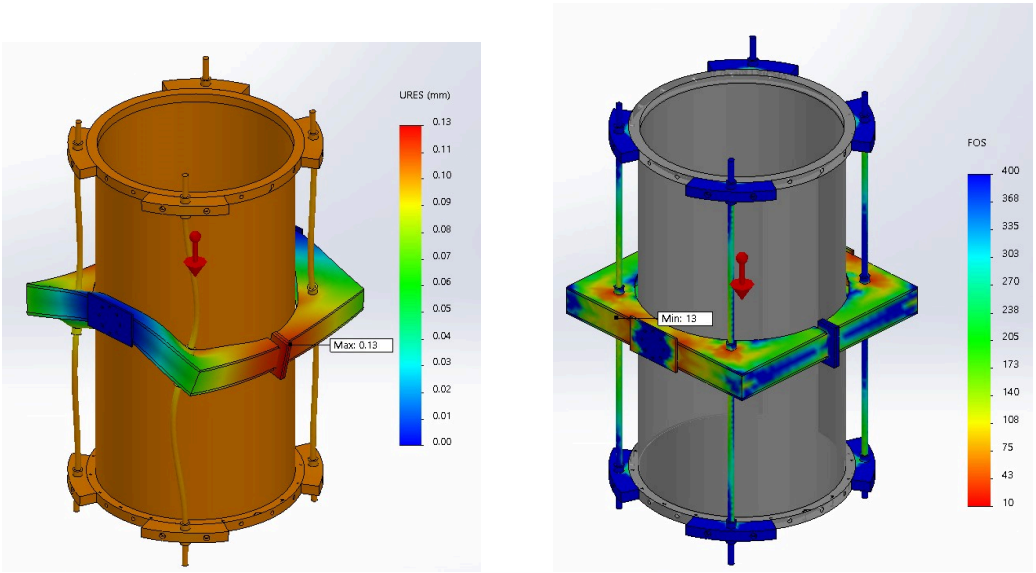

(a) **(b)**

Figure 2.3.3: Displacement **(a)** and factor of safety **(b)** analysis for the v0-0° configuration.

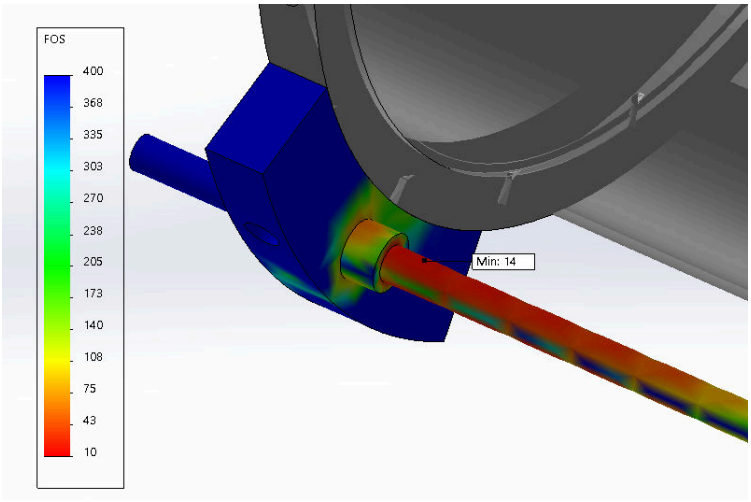

Figure 2.3.4: Factor of safety analysis for the v0-90° configuration

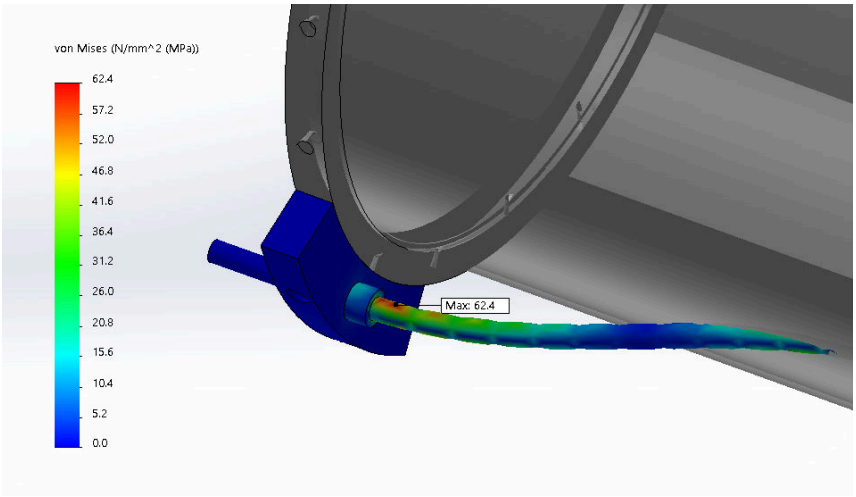

(a)

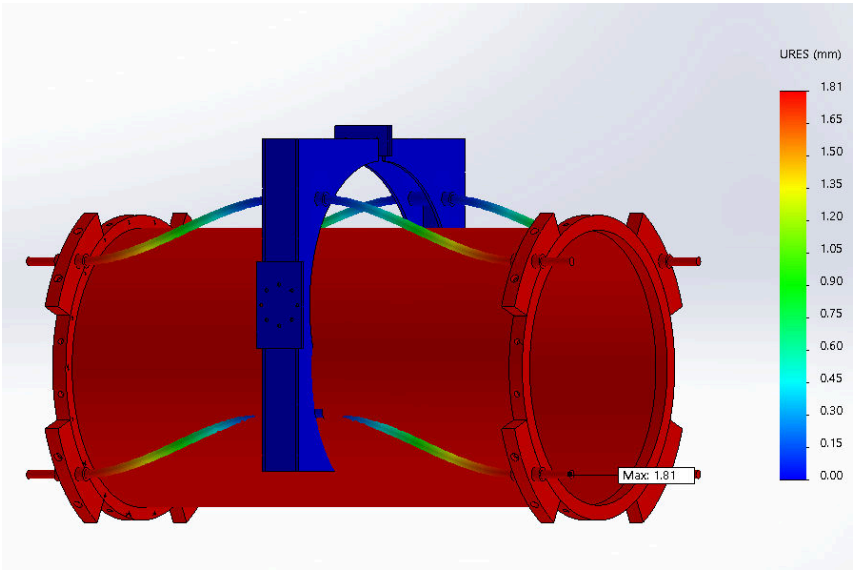

(b)

Figure 2.3.5: Von Mises stress **(a)** and displacement **(b)** analysis for the v0-90° configuration.

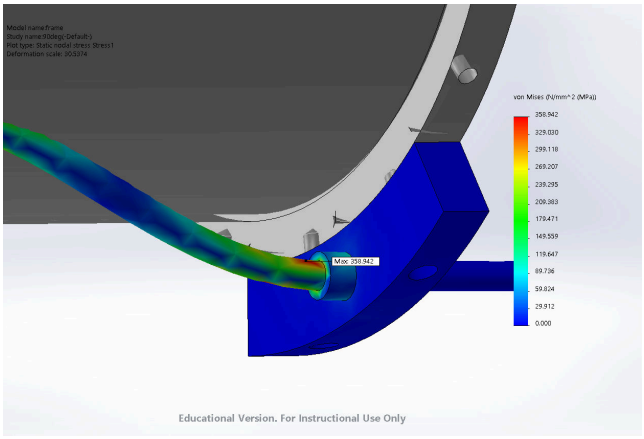

(a)

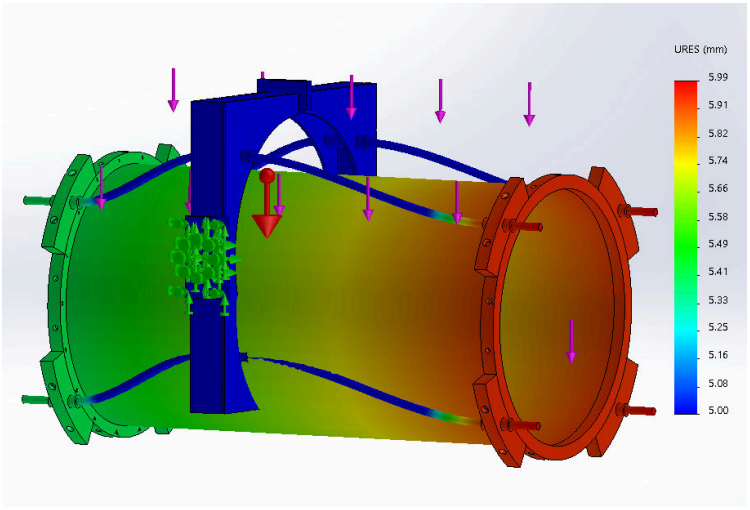

(b)

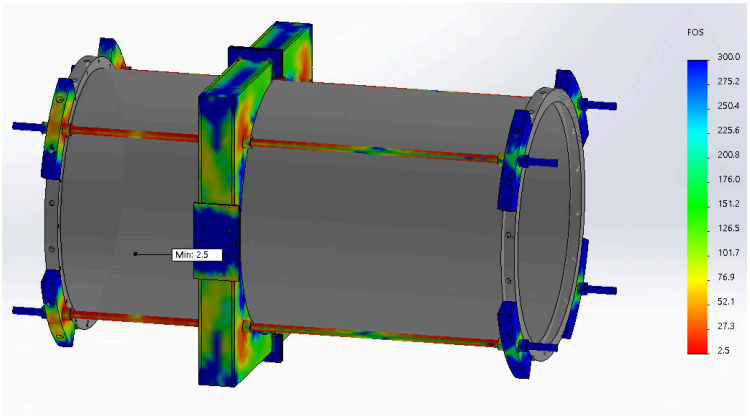

(c)

Figure 2.3.6: Von Mises stress **(a)**, displacement **(b)** and factor of safety **(c)** analysis for the v0.1-90° configuration.

2.3.2 v1 frame simulations

The assumptions and approximations in this run were the same of the previous one, with the fixtures placed on the hinges' plates and the dummy cryostat treated as a rigid body. Given the fact that the v0 structure had passed the simulations in the vertical configuration, for this version only the horizontal configuration has been simulated; the results are reported in Table 2.3.4 and in Figure 2.3.7.

Inclination (deg)	**90**
Max Von Mises stress (MPa)	107.318
Max displacement (mm)	1.564
Min factor of safety	8

Table 2.3.4: Results of the static analysis of the v1 configuration.

2.3.3 v1 frame+mount static simulations

In this run the frame was simulated onto the AzEl mount: to simplify the simulation only the upper part of the mount was considered (the base has been simulated separately and the results are presented in Section 2.5). The fixtures were placed at the bottom of the mount, as shown in Figure 2.3.8, and in addition to the dummy cryostat, also the hinges on the top of the mount were considered rigid. Six configurations were analyzed, respectively with the cryostat at $0°$,$15°$,$20°$,$30°$,$45°$,$90°$ from the vertical axis of the mount.

The results of this study are summarized in Table 2.3.5, while all the Figures are reported in Appendix A.1.

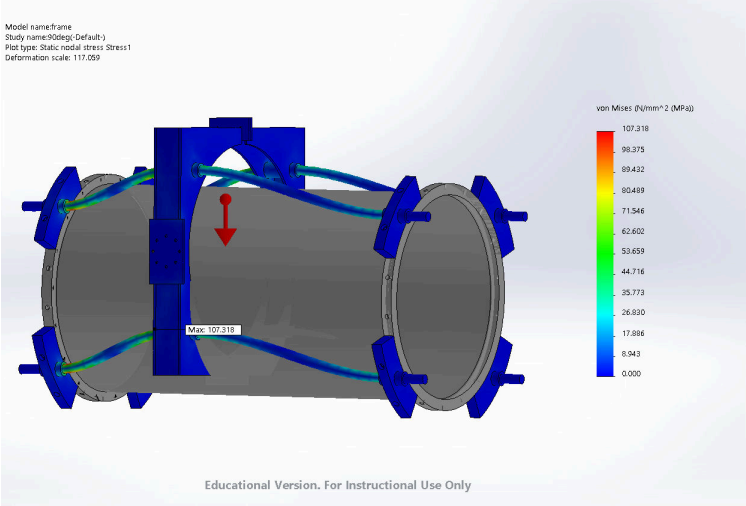

(a)

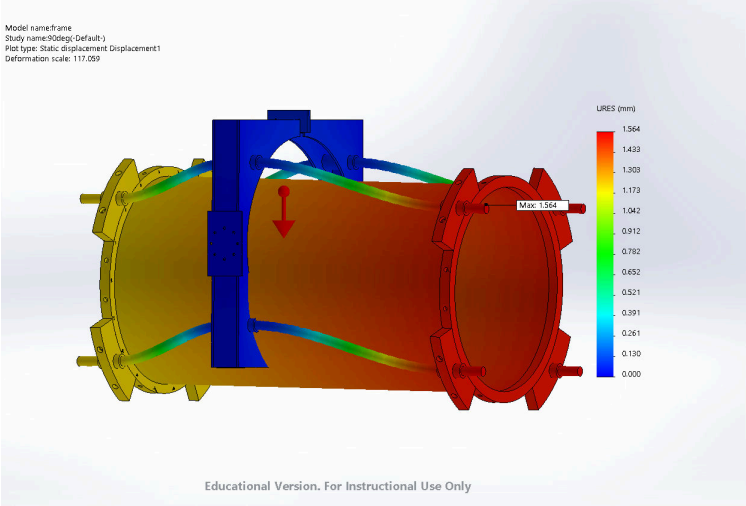

(b)

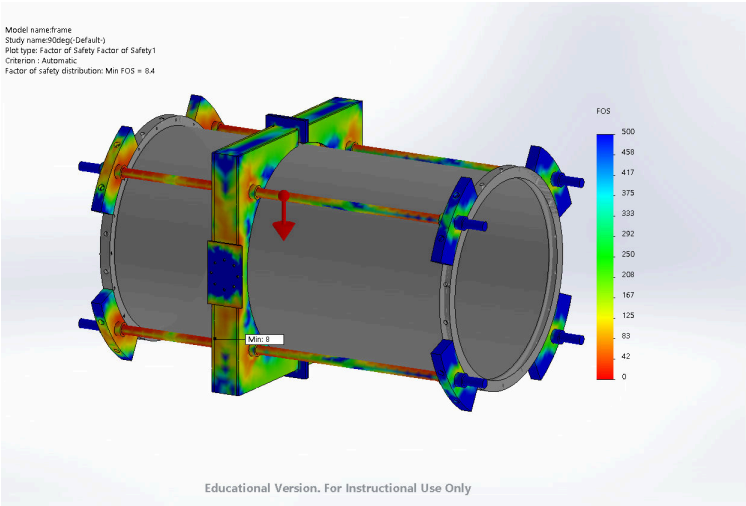

(c)

Figure 2.3.7: Von Mises stress **(a)**, displacement **(b)** and factor of safety **(c)** analysis for the v1-90° configuration.

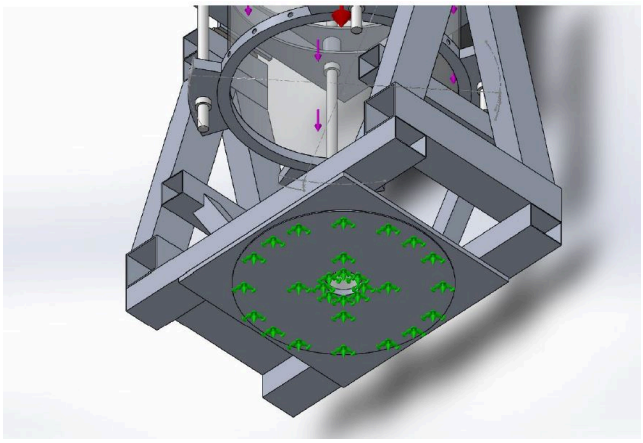

Figure 2.3.8: Location of the fixtures in the v1 *frame+mount* simulations.

Inclination (deg)	0	15	20	30	45	90
Max Von Mises stress (MPa)	38.9	46.8	51.9	69.0	87.8	111.2
Max displacement (mm)	0.58	0.94	1.15	1.58	2.15	2.83
Min factor of safety	7	6	7	8	6	5

Table 2.3.5: Results of the static analysis of the v1 frame + mount.

In the $0°$, $15°$, $20°$ configurations the maximum stress is experienced by the plates attached to the trunnions; as shown in Figure 2.3.9 in the $30°$ and $45°$ configurations the maximum stress is instead on the lower side of the rods (tilt side), just below the square frame; the maximum displacement happens always on the top of the cryostat, except for the $0°$ configuration for which it is on the bolted edge of the square frame; except for the $90°$ configuration, the point with minimum factor of safety always lies on the connection between the frame and the trunnions.

In order to estimate the distortion induced in the beam map, for each configuration the displacement values were converted into angular deviation of the telescope axis: the relation between this deviation and the inclination angles is reported in Figure 2.3.10. At 30 and 40GHz respectively BICEP

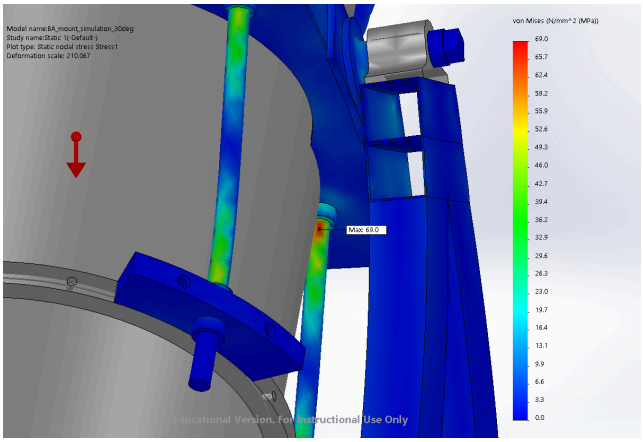

Figure 2.3.9: Detail of the area of maximum stress in the 30° configuration.

Array has an angular resolution of 1.40° and 1.05°, while in the worst case scenario the deviation is 0.003°, so the distortion induced by this angular deviations would be largely negligible in the beam map process.

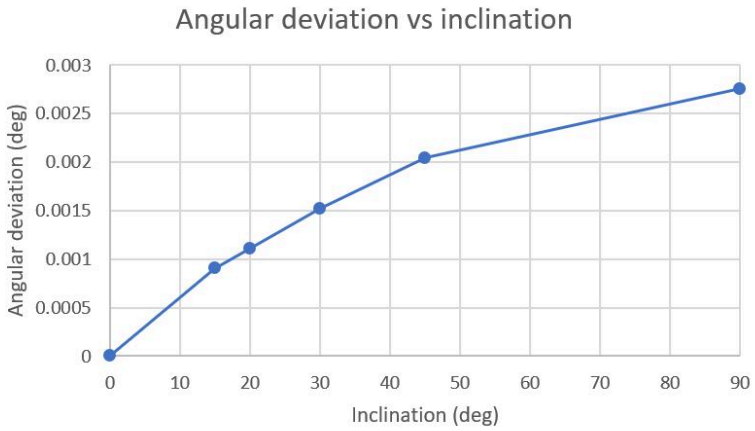

Figure 2.3.10: Trend of how the receiver axis deviates from its nominal position against its inclination.

The minimum factors of safety obtained are always above 1 and although they are not so high, it has to be reminded that they were obtained using a test mass 1.5 times higher than the nominal one; nevertheless, this study

needs to be refined with a more detailed mass budget and with the addition of the mirror structure described in Section 2.4.

2.3.4 v1 frame+mount buckling simulations

In this case also buckling simulations were performed, as there was more interest in characterizing the stability of the complete structure. Six modes of instability have been simulated for each configuration; the results are shown in Appendix A.2, while the resulting load factors for each buckling mode are summarized in Table 2.3.6.

Inclination (deg)	0	15	20	30	45	90
Mode 1	25.0	26.5	26.8	26.9	37.2	27.0
Mode 2	28.2	29.7	29.6	29.5	40.1	28.6
Mode 3	29.0	29.7	29.7	29.9	40.1	28.7
Mode 4	46.8	47.7	48.0	48.8	69.3	52.8
Mode 5	97.0	95.9	94.7	91.8	120.0	81.7
Mode 6	110.9	108.5	106.2	101.0	128.2	83.4

Table 2.3.6: Results of the buckling analysis of the v1 frame + mount: for each configuration the load factor of each buckling mode is shown.

The main information gained from the buckling analysis is that the most of the instability resides in the two beams on the top of the A-structure of the mount: all the loads needed to produce these instabilities are several times higher than the nominal load, but it would anyway be a safer option to put two aluminum plates on the sides of the beams in order to make the structure more solid, as done for the v2 version of the interface frame.

2.4 DESIGN OF THE FAR FIELD FLAT (FFF) MIRROR

As stated in Chapter 1, far-field beam calibration of the 30/40GHz receiver requires that the source is $\sim 70m$ away from the instrument. Unfortunately, having to put the source so far away without having the possibility to going too much up in height means that the receiver should point at an object very low in elevation: this represents a limit because the cryostat's fridge is not built to work at very large levels of inclination. BICEP Array has a FOV of about $30°$: using a flat folding mirror in a way that the source is in the center of the FOV when the cryostat is in vertical position, would reduce the required scanning in elevation down to only $\sim \pm 15°$ away from the vertical axis. Moreover, the beam calibration will take place in Caltech's High Bay, which is a shared space: as visible in Figure 2.4.1, the line of sight between the source and the mount is blocked by instrumentation of other research groups, so a flat folding mirror placed over the cryostat is needed in order to have a clear line of sight and perform the beam mapping.

A preliminary design was proposed, basing on the following drivers:

1. must contain all *FOV* with 2" tolerance
2. *location* (elevation) of the source
3. *lightweight* but *solid* structure
4. inclination *adjustability*

Two different concepts were considered:

- *alt-az following* - the structure holding mirror would be attached on the same frame that holds the cryostat, following its movement along both azimuth and elevation axes (Figure 2.4.2a).

Figure 2.4.1: Caltech's High Bay: the source will be located on the balcony marked by the red arrow, which is partially hidden by the instrumentation used by other experiments.

- *only-az following* - the mirror would be linked directly on the mount, following the movements only along the azimuth axis.

The two concept have both advantages and disadvantages: the first one would provide a more compact mirror (easier to make) where the FOV scans always the same spot (reducing systematics), at the cost of putting more stress on the cryostat frame and adding counterweights to balance a load far above the elevation axis; in the second concept the load would be applied directly on the mount, without stressing the structure and with no need for counterweighting, at the cost of making a bigger mirror ($\gtrsim 3m$) which would be scanned by the FOV in different areas for each different elevation angle.

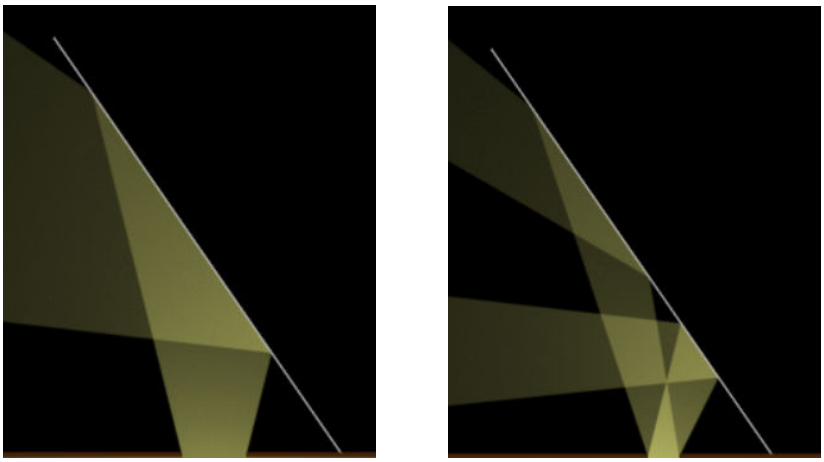

(a) Alt-Az following **(b)** Only-Az following

Figure 2.4.2: Graphic sketch of the FOV coverage for the two different mirror concepts: in the case (a), while working at different elevation angles the FOV scans always the same area on the mirror; in the case (b) the FOV covers different areas on the mirror when changing the elevation angle.

Seen from the top of the cryostat the source is located at an elevation of $\sim 13^\circ$ so, doing calculations with a more conservative[4] value of 15°, in order to have the source centered in the FOV when the cryostat is in vertical position the mirror needs to be tilted by 52.5° with respect to the floor, as shown in Figure 2.4.3.

During *BICEP3* beam calibration operations at Harvard it was used a mirror which followed the telescope in both azimuth and elevation (see Figure 2.4.4, so our mirror was designed using heritage from that design, adopting the first of the two concepts.

The preliminary design resulted in a 210x130x$6cm$ aluminum mirror of $\sim 75Kg$: the mass estimate has been done considering a honeycomb core with $\sim 10\%$ the density of aluminum (following Harvard's mirror specifications).

4 The larger the angle of tilt, the harder it is to contain the whole FOV.

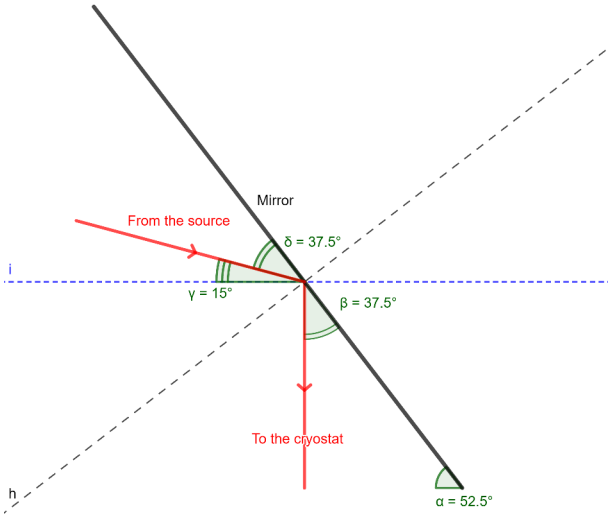

Figure 2.4.3: Graphic sketch of the optical path: in order to have the source in the center of the FOV when the cryostat is in vertical position the mirror needs to be tilted by $52.5°$.

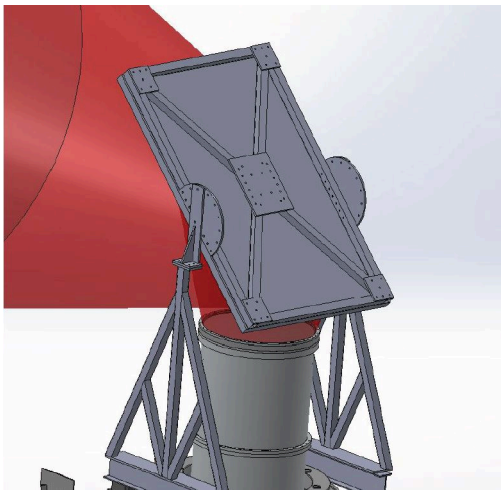

Figure 2.4.4: CAD design of the Far Field Flat used at Harvard for far field beam calibration.

The two plates located on the mirror's sides would be used to make small adjustments of the inclination. The A-structure that holds the mirror is made of commercial aluminum railings connected together by aluminum

plates, for an estimated weight of $\sim 80Kg$. The mirror will be located at a minimum distance of $5.6cm$ over the cryostat's window. Both the mirror and the structure are shown in Figures 2.4.5 and 2.4.6.

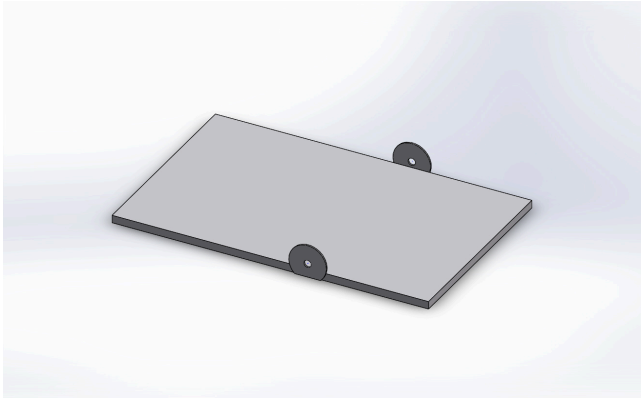

Figure 2.4.5: CAD drawing of the mirror.

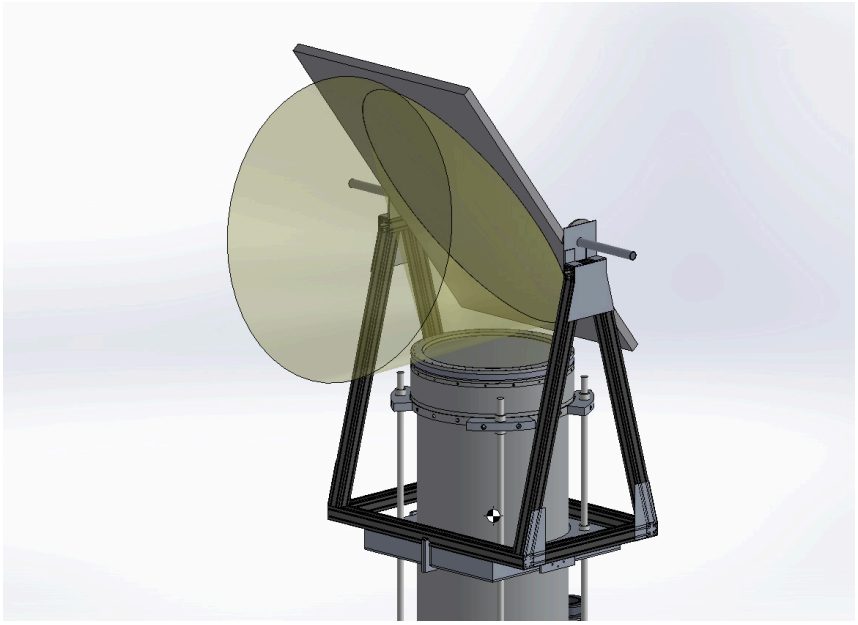

Figure 2.4.6: CAD drawing of the structure that holds the mirror above the cryostat.

The choice of this concept raised the need for counterbalancing the additional weight that was put on the cryostat's frame, in order to have the

	dx(mm)	dy(mm)
Without counterweights	6	368
With counterweights	5	278

Table 2.4.1: Position of the center of mass relative to the elevation axis.

center of mass (CoM) lying on the elevation axis: as reported in Table 2.4.1 and Figure 2.4.7 the addition of counterweights is not sufficient to place the CoM on the elevation axis, or at least close to it (the elevation motor can work with deviations of the CoM from the elevation axis up to 1"). Although the results of this preliminary study are not satisfactory, the mass budget of the cryostat has still to be refined so this analysis will have to be done again with a more detailed design.

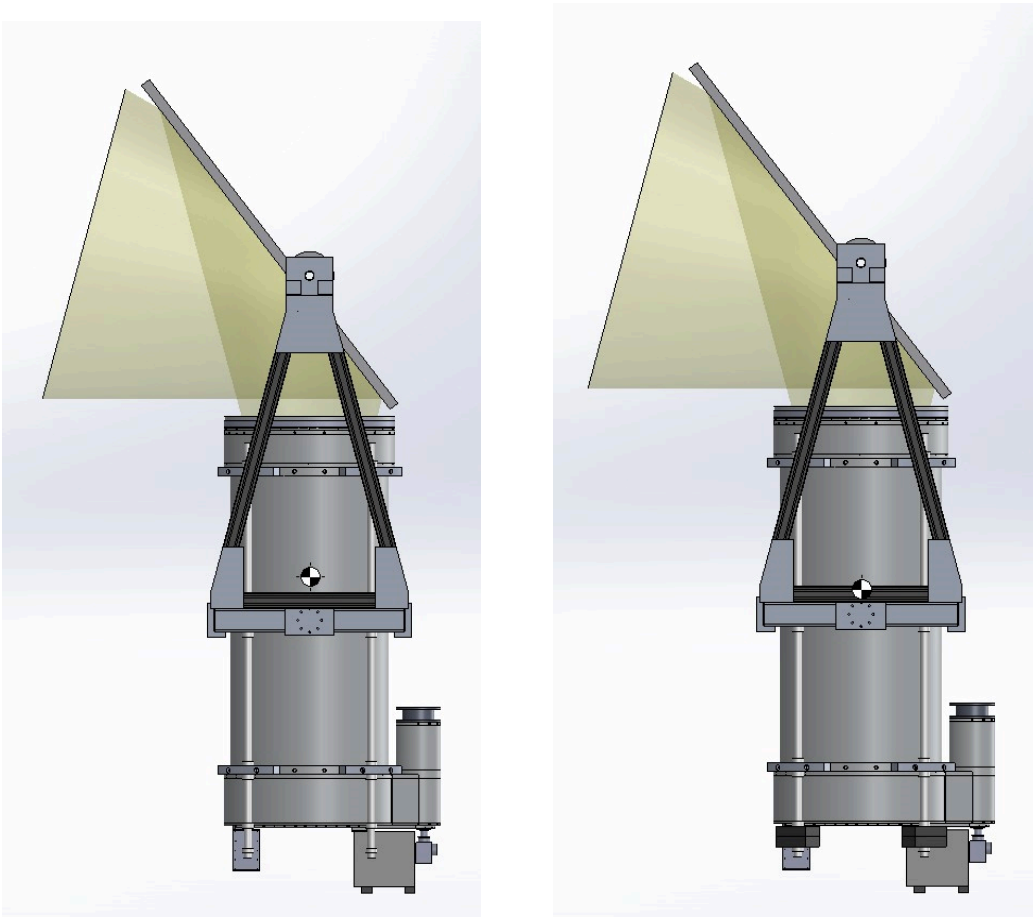

(a) No counterweights **(b)** With counterweights

Figure 2.4.7: Changes in the position of the center of mass without **(a)** and with **(b)** counterweights.

2.5 SIMULATIONS OF THE AZEL GADGET BASE

It was chosen to run the simulations of the base separately to reduce the complexity of the simulations: this way the only part of the mount which has not been simulated is the azimuth bearing, which is a really complex part to simulate but which can hold up to $19000Kg$ according to its specifications, so it has been considered safe. The base assembly is shown in Figure 2.5.1.

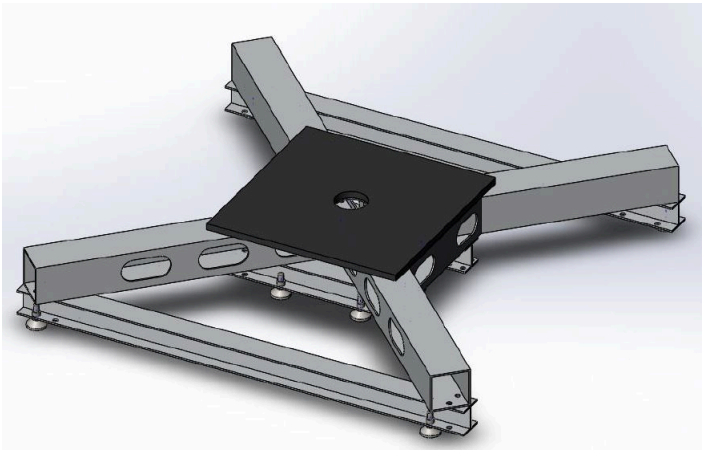

Figure 2.5.1: CAD assembly of the base.

A load of $1330Kg$ (accounting for the top part of the mount, the interface frame and the cryostat) has been applied on the top plate of the mount, and also gravity has been taken in account; the fixtures were placed on the bottom of the feet (see Figure 2.5.2). As for the mount interface, static simulations were performed to study stresses, displacement, and the factor of safety.

Currently the base stands on eight feet located as shown in Figure 2.5.3 a; apart from this one (which will be called v0), other two configurations have

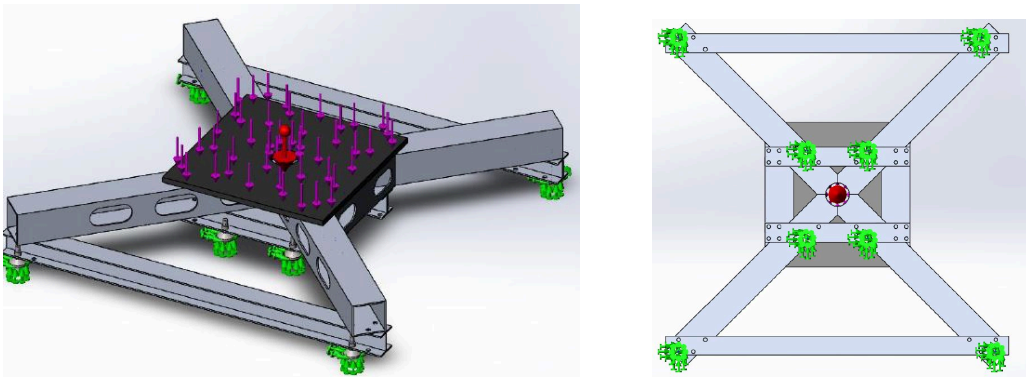

(a) **(b)**

Figure 2.5.2: Loads **(a)** and fixtures **(b)** used for the simulations of the base.

been studied: one obtained moving the inner feet (v1), and another one obtained adding four feet (v2).

Each of the feet can support a $2500Kg$ load, but it was chosen to try a configuration with four additional feet in order to better distribute the load and reduce the stress on the aluminum beams that make the structure.

The results of the simulations are reported in Table 2.5.1, and in the Figures A.3.1, A.3.2, A.3.3: the highest stress is expected on the aluminum beams in correspondence with the feet, hence the addition of four more feet can mitigate this behavior.

Configuration	v0	v1	v2
Max Von Mises stress (MPa)	68	62	35.17
Max displacement (mm)	0.13	0.14	0.08
Min factor of safety	3	3	5

Table 2.5.1: Results of the static analysis of the v0 configuration.

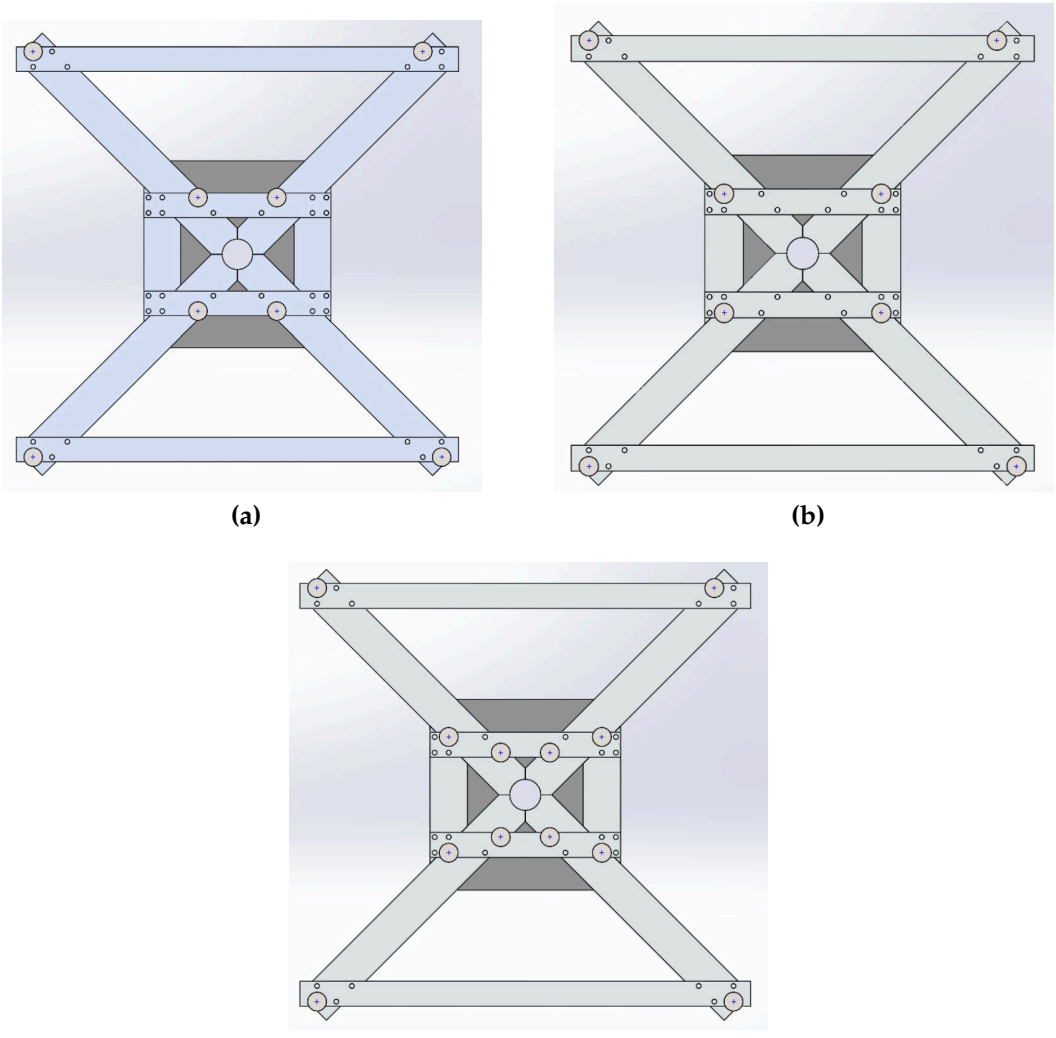

(a) **(b)**

(c)

Figure 2.5.3: Bottom view of the three different configurations which have been studied: current one v0-**(a)**; moving the existing feet v1-**(b)**; adding four feet v2-**(c)**.

3 HOUSEKEEPING BOX

Part of this summer internship was focused on the design of a warm electronics junction box to be used during beam characterization operations at Caltech.

The purpose of this component is to better organize the cables which control the thermometry system of the cryostat (i.e. thermometers, heat switches, heaters): the box takes the inputs from five 100 pin micro-D connectors placed on the bottom of the cryostat and then splits these channels among ten D-subs connectors, used for the thermometers, and thirty BNC connectors, used for the heaters. For reference, a scheme of the housekeeping system is shown in Figure 3.0.1:

The main drivers of the design of this box were light weight and low-costs; also, a secondary driver was the compatibility of the box with all of the four receivers of the array. The box assembly is shown in Figure 3.0.2.

As shown in Figure3.0.3 the box consists of:

- base plate - needed to attach the box to the cryostat without unmounting all the sides each time one has to remove/attach the box. This base plate also has six holes on the sides for additional pieces which will provide support for the readout electronics of the 150GHz receiver

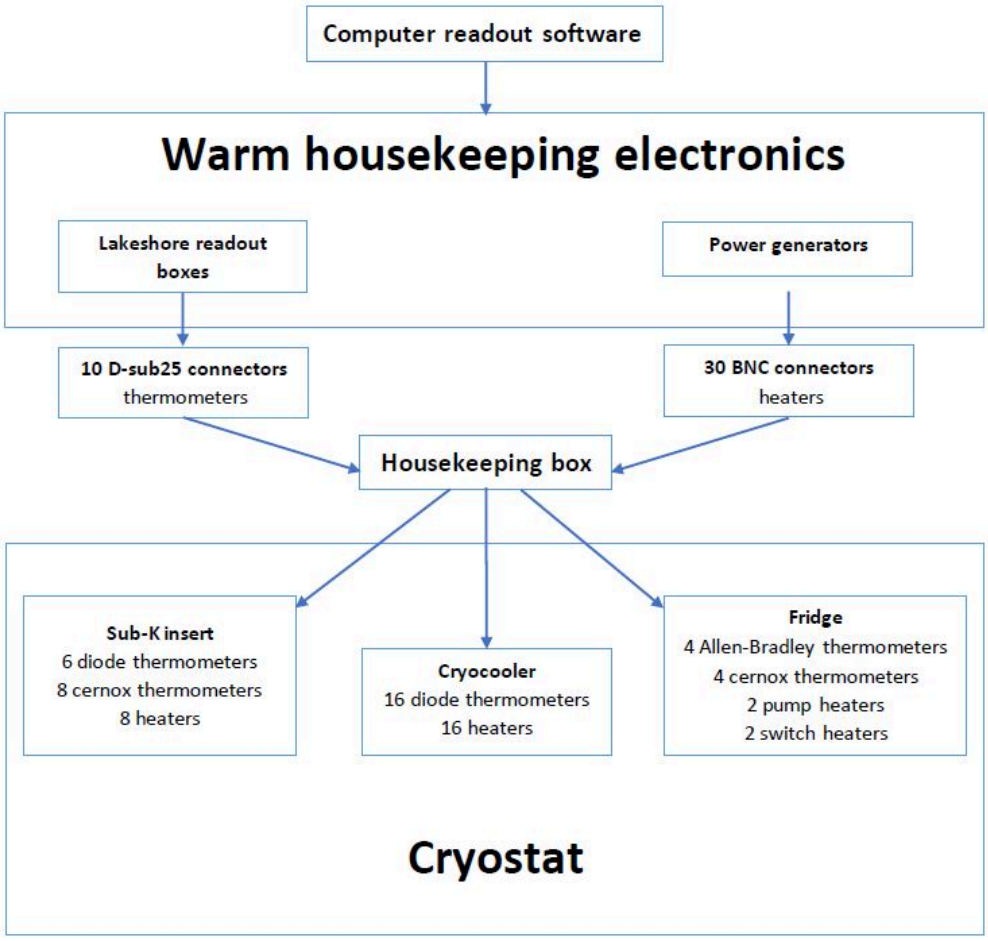

Figure 3.0.1: Housekeeping system block diagram.

- bottom plate - this part is directly mounted on the base plate, and has an hole which provides access to the connectors on the cryostat
- four rail standoffs - these parts connect the bottom and the top plate, holding in place also the sides of the box
- side walls - the sides are made of 1.6mm thick aluminum sheets; these parts were made in Caltech's machining shop, as were the holes for

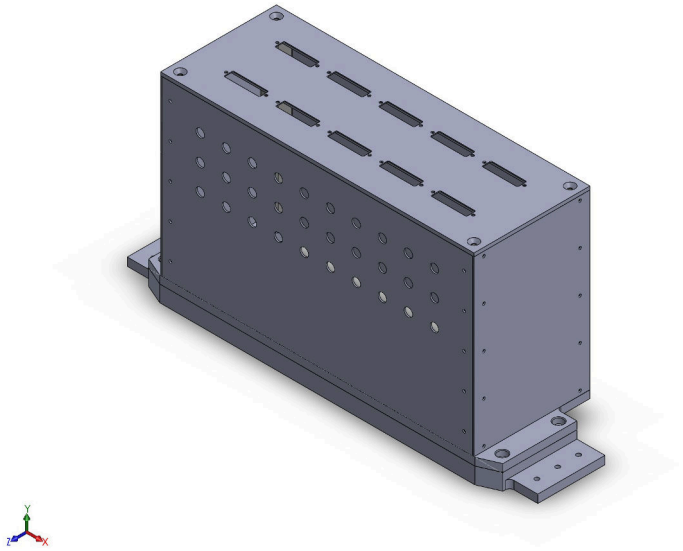

Figure 3.0.2: Housekeeping box: here are clearly visible the holes for the ten d-subs connectors and for the thirty BNC connectors. The model is shown in isometric projection.

the standoffs screws and for the BNC connectors; a view of the wall hosting the BNCs is presented in Figure 3.0.4

- top plate - this plate is attached to the four standoffs and it hosts the ten 25 pin D-sub connectors

Part of this work involved also making the cables which go from the cryostat connectors to the BNC and D-sub outputs hosted on the box. As visible in Figure 3.0.6, all the wires were twisted in pairs both for shielding from RF interferences and for easing the labeling process. The fully assembled box is shown in Figure 3.0.7.

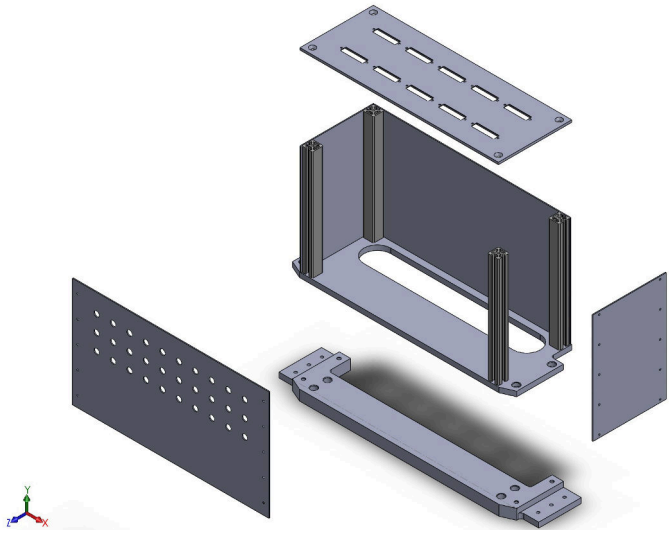

Figure 3.0.3: Exploded view of the Housekeeping box which shows the internal standoffs and the bottom plate. The model is shown in isometric projection.

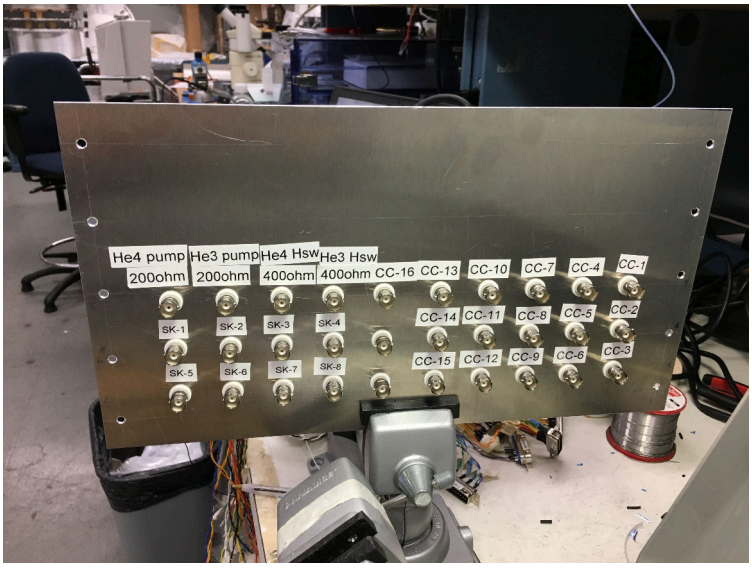

Figure 3.0.4: View of the BNC connectors hosted on one side of the box.

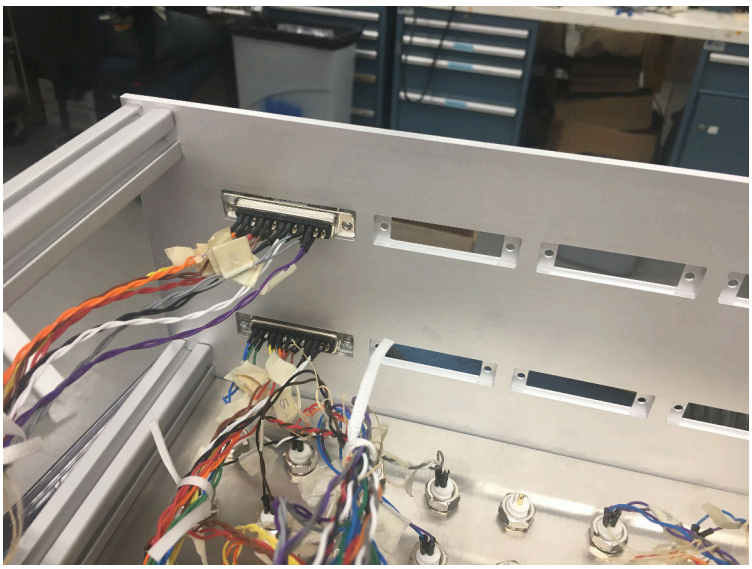

Figure 3.0.5: View on the back of the top plate: this perspective shows the slots extruded in the plate to host the D-subs connectors.

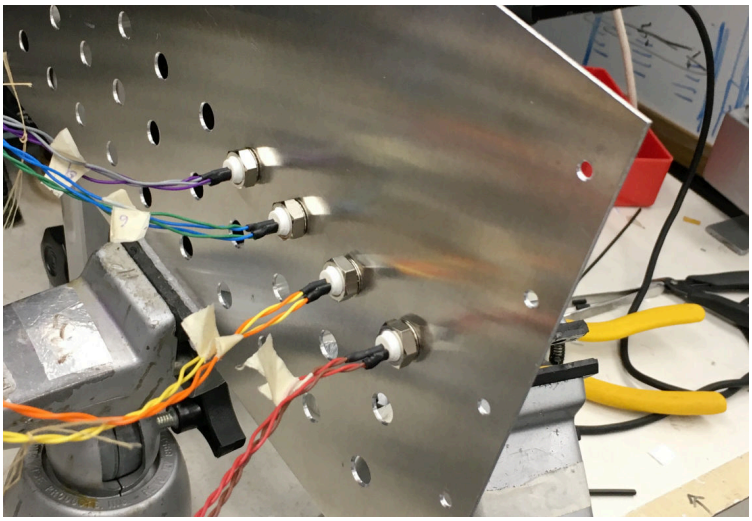

Figure 3.0.6: Close-up view on the back of a few BNC connectors: the pair-twisting of the wires is clearly visible.

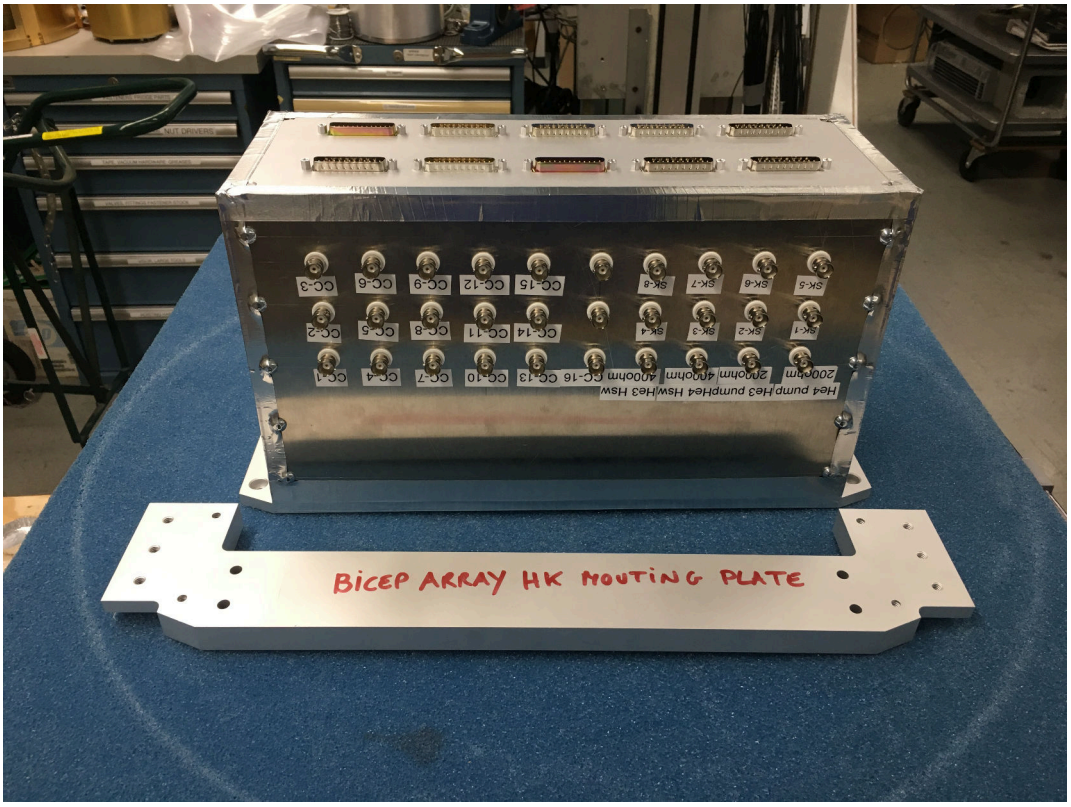

Figure 3.0.7: The completed box, with the mounting "base" plate in foreground.

CONCLUSIONS

The design and the preliminary simulation study on the AzEl mount interface for BICEP Array conducted during this internship represent a good starting point for what will come next in preparing the beam calibration tests: both the base and the fork of the AzEl mount reacted well to the solicitations expected from the load of the receiver, and a draft design of an interface frame has been produced. On the other side, a deeper structural analysis is required while parameters like the mass budget will surely be refined; a dedicated study on the other mirror concept should be the best option in the eventuality that the new mass estimates will not result in a position of the center of mass close enough to the elevation axis.

A warm housekeeping box has been designed, built and then used during the first cryogenic run of the 30/40GHz receiver.

Although not included in this report, two weeks of this internship were dedicated to the integration of the receiver in Caltech's high bay: I took part in the installation of the fridge and of the magnetic shield, for which I also wrote a small internal document describing the installation procedure.

A | SIMULATIONS FIGURES

A.1 V1+MOUNT STATIC

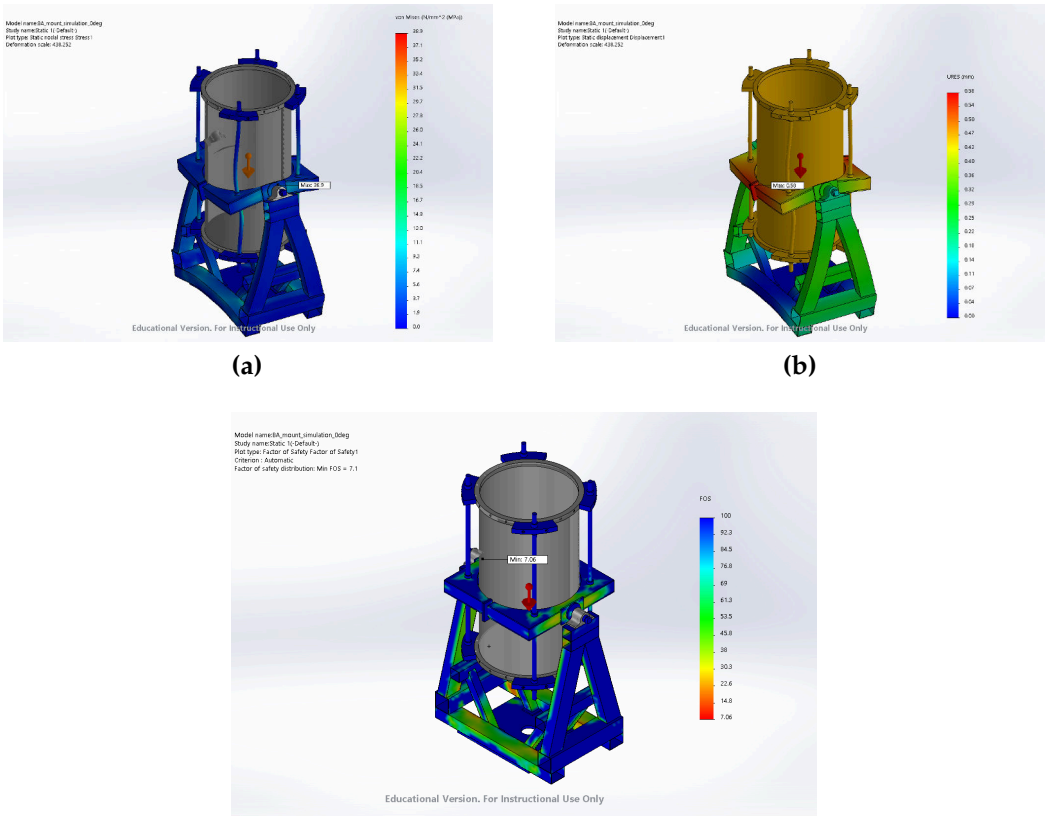

(a) **(b)**

(c)

Figure A.1.1: Static simulations of the 0° configuration: Von mises stress **(a)**, displacement **(b)** and factor of safety **(c)**.

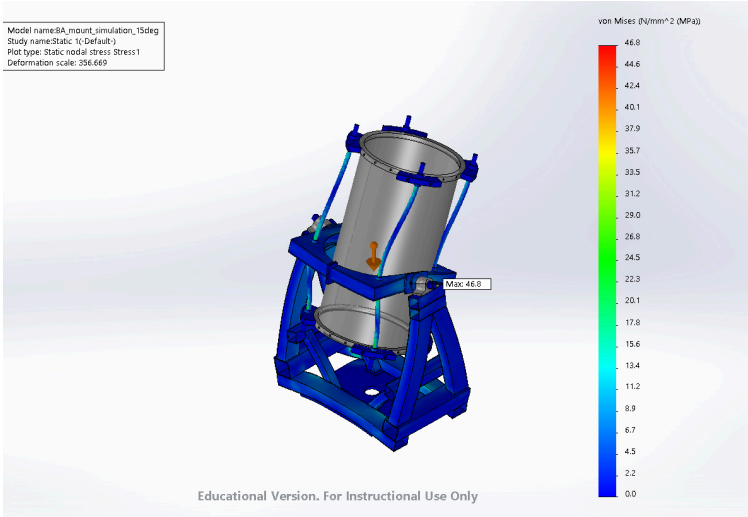

(a)

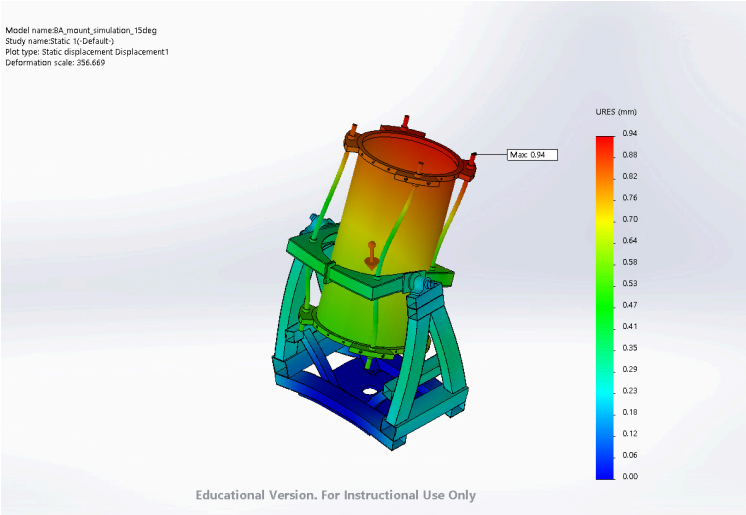

(b)

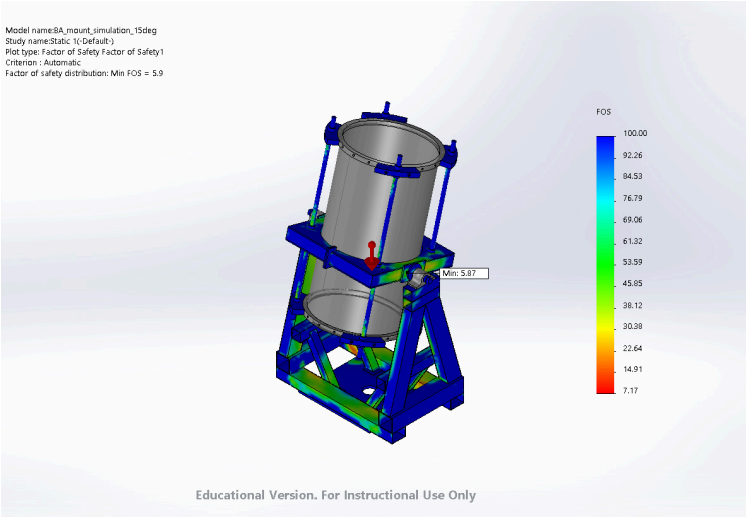

(c)

Figure A.1.2: Static simulations of the 15° configuration: Von mises stress **(a)**, displacement **(b)** and factor of safety **(c)**.

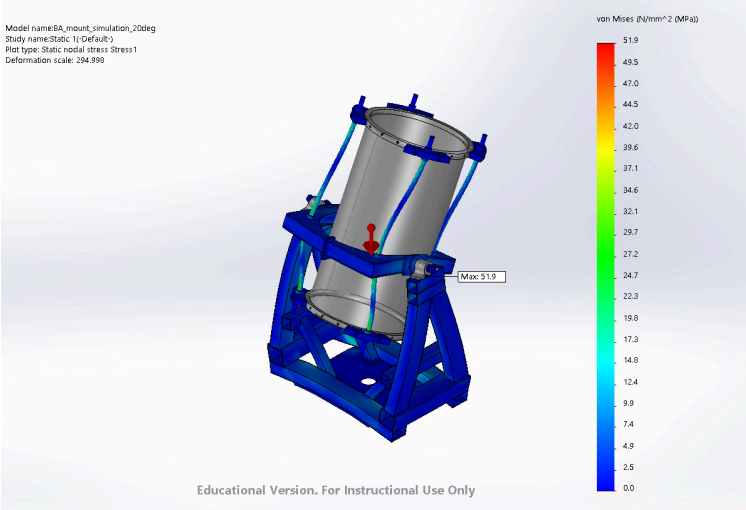

(a)

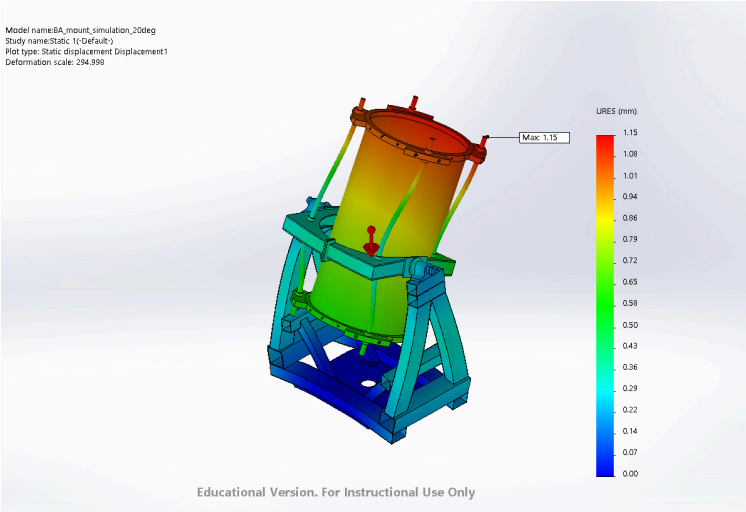

(b)

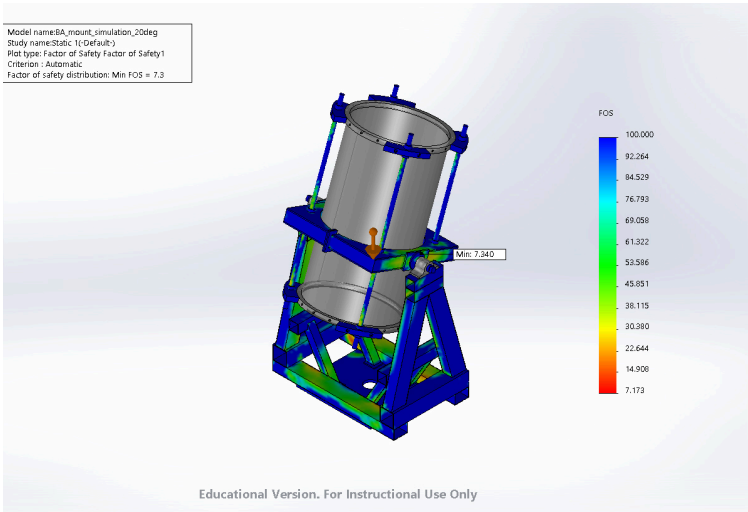

(c)

Figure A.1.3: Static simulations of the 20° configuration: Von mises stress **(a)**, displacement **(b)** and factor of safety **(c)**.

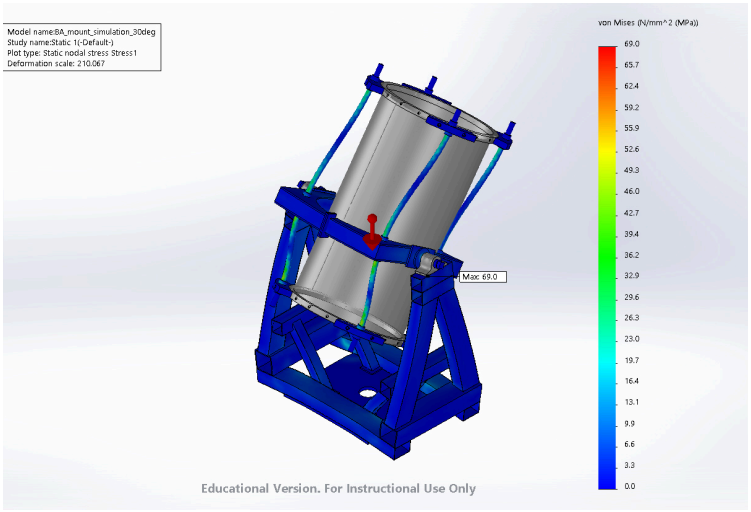

(a)

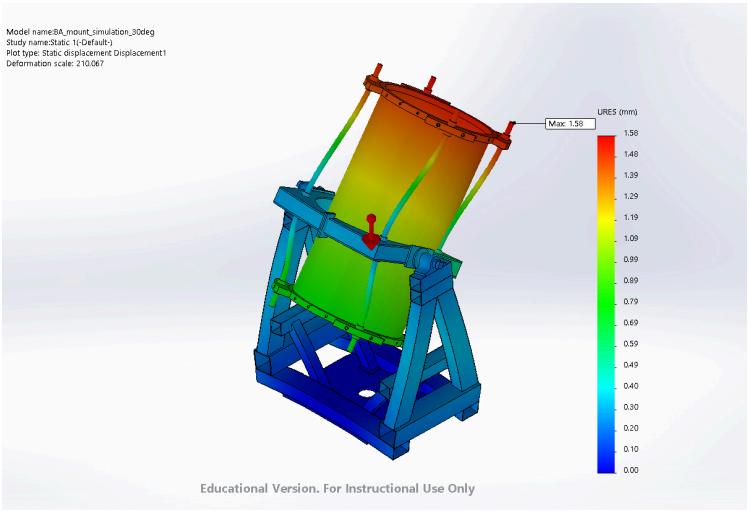

(b)

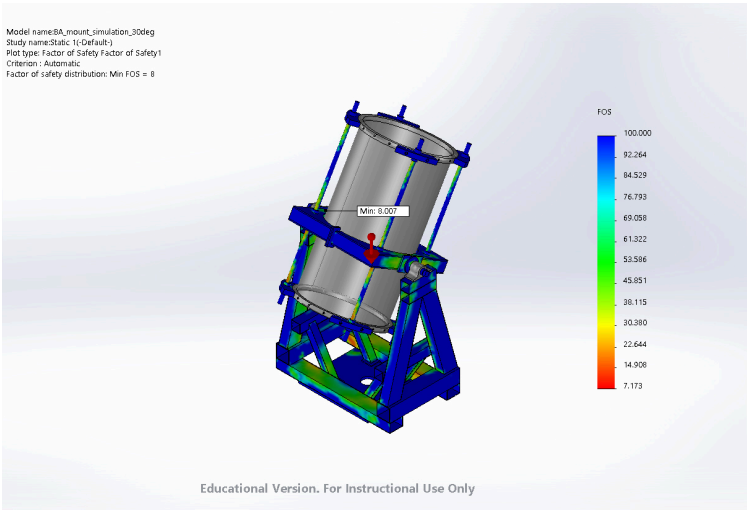

(c)

Figure A.1.4: Static simulations of the 30° configuration: Von mises stress **(a)**, displacement **(b)** and factor of safety **(c)**.

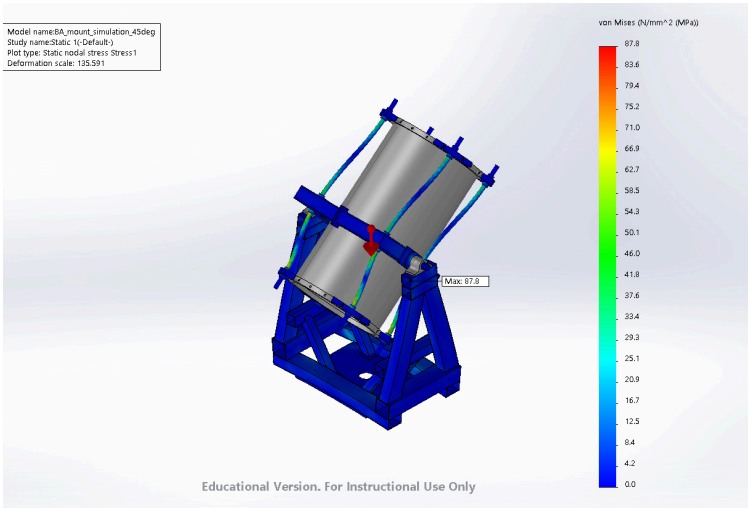

(a)

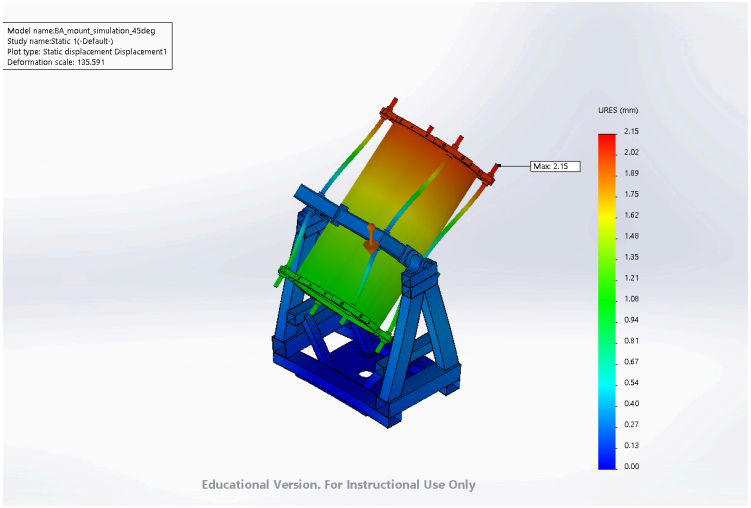

(b)

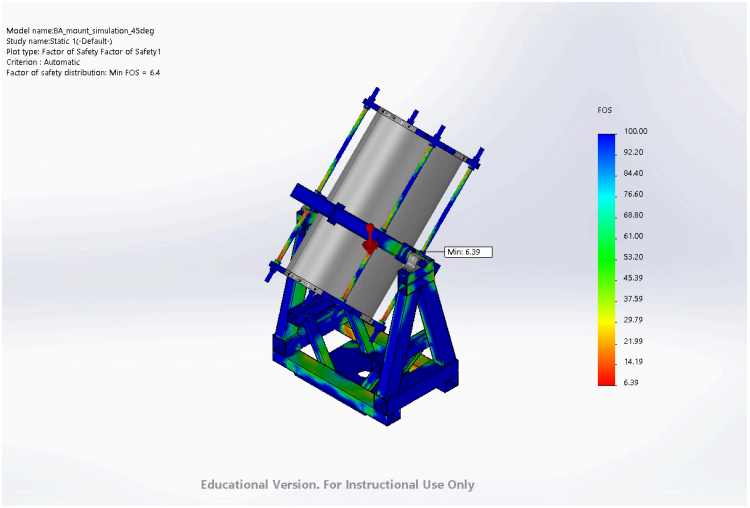

(c)

Figure A.1.5: Static simulations of the 45° configuration: Von mises stress **(a)**, displacement **(b)** and factor of safety **(c)**.

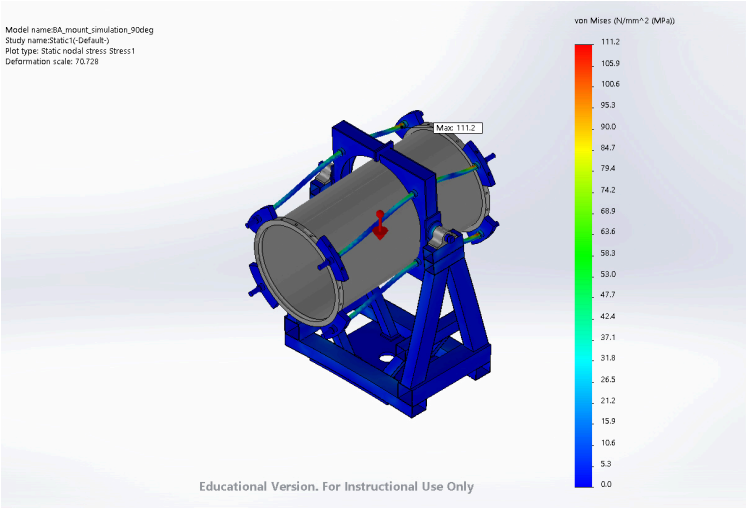

(a)

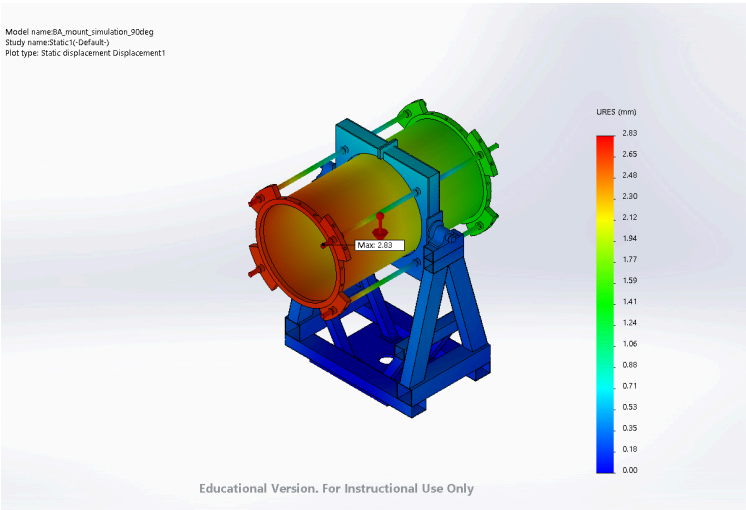

(b)

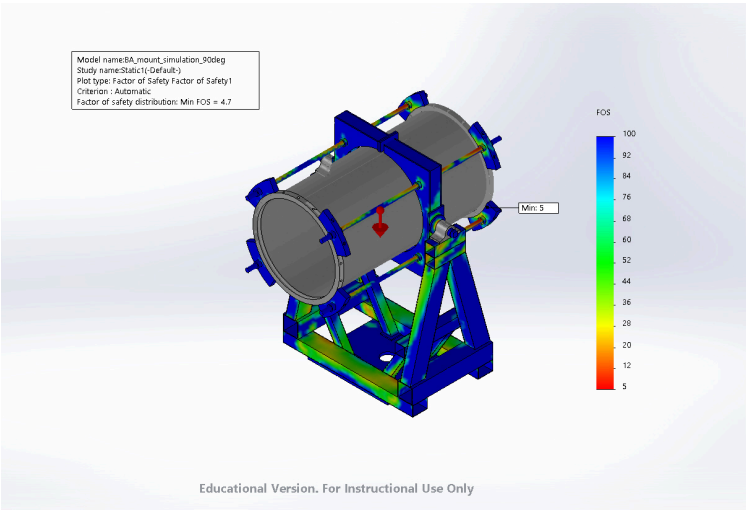

(c)

Figure A.1.6: Static simulations of the 90° configuration: Von mises stress **(a)**, displacement **(b)** and factor of safety **(c)**.

A.2 V1+MOUNT BUCKLING

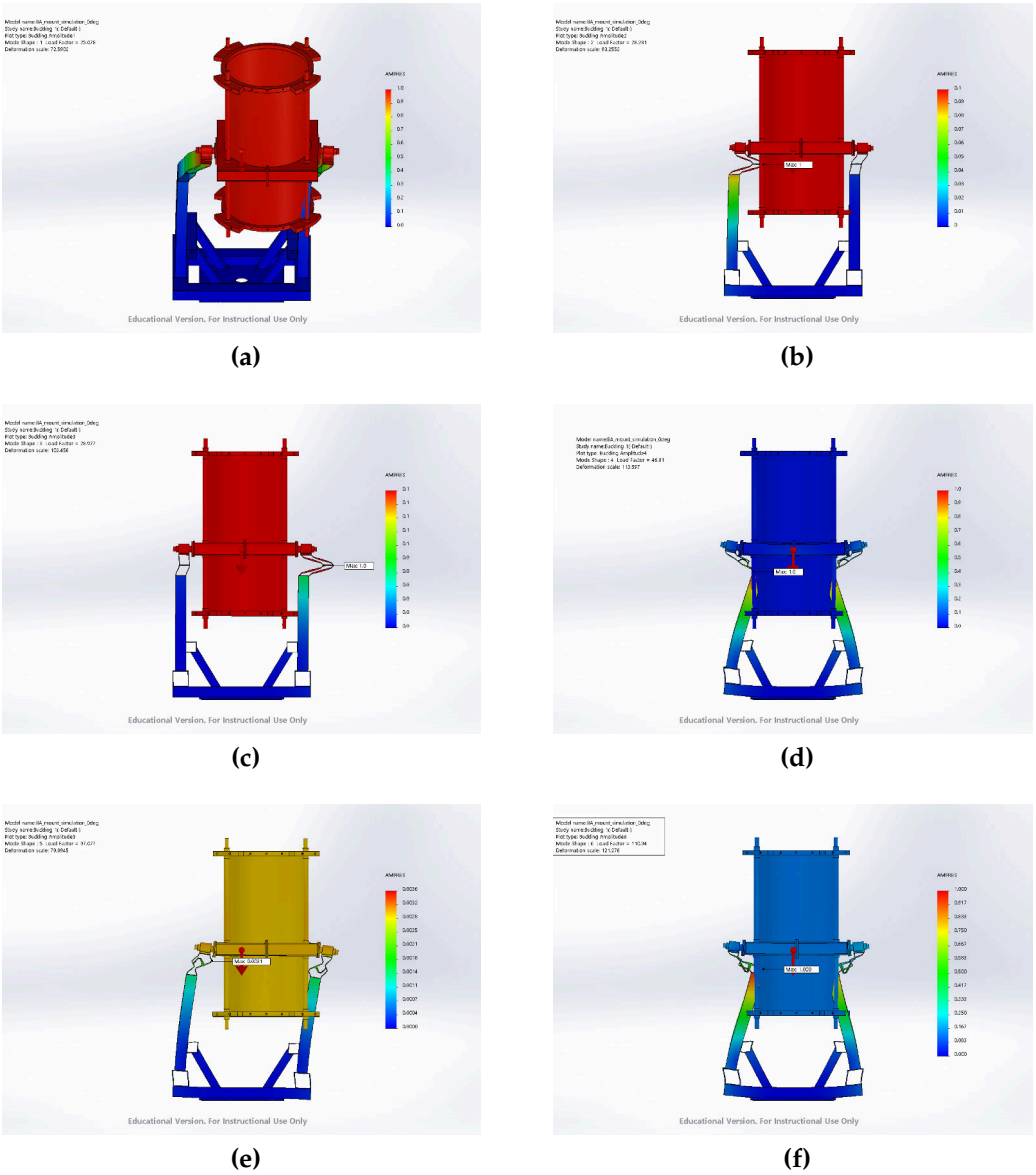

Figure A.2.1: Buckling simulations of the 0° configuration: 1st mode **(a)**, 2nd mode **(b)**, 3rd mode **(c)**, 4th mode **(d)**, 5th mode **(e)**, 6th mode **(f)**.

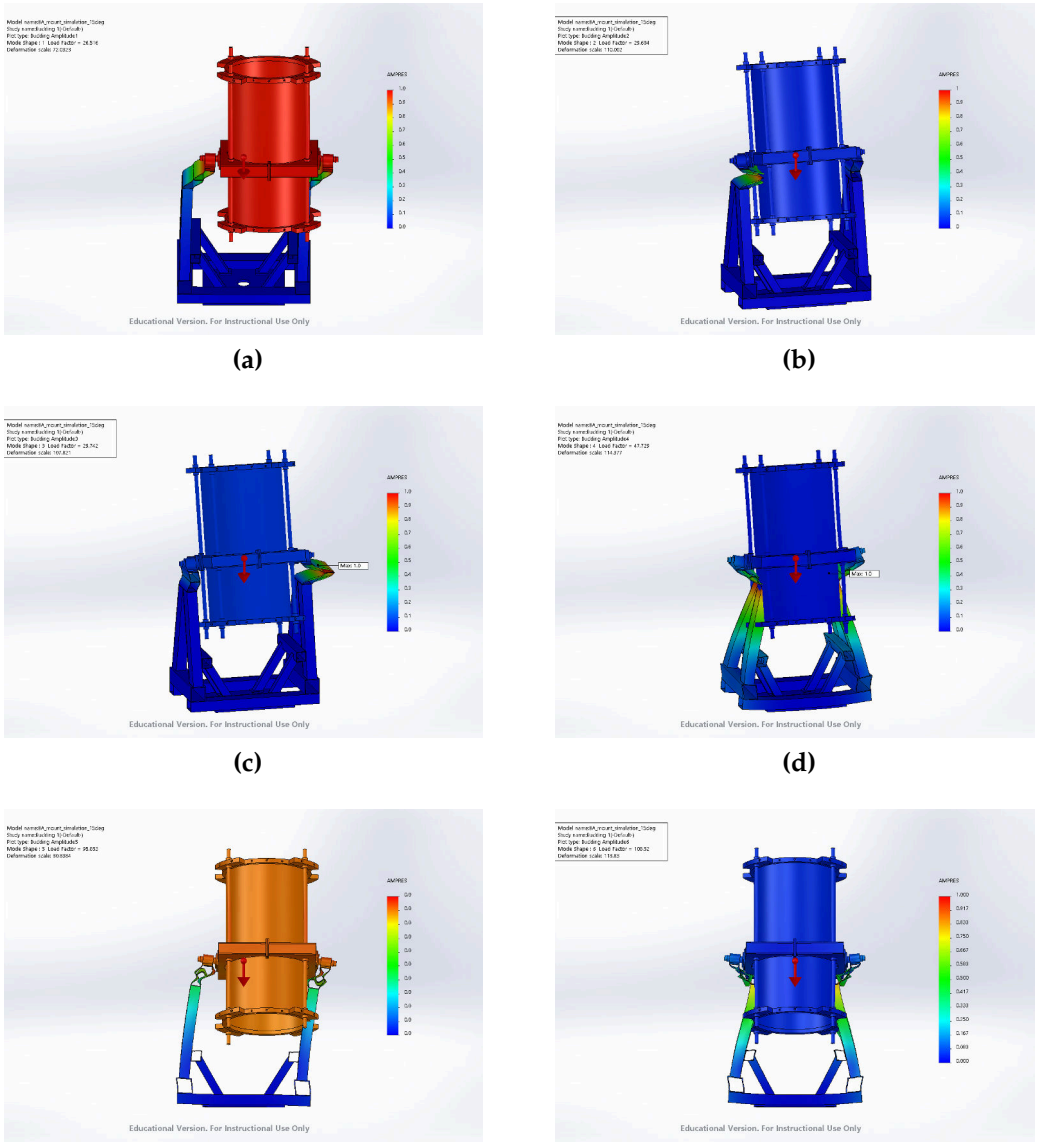

Figure A.2.2: Buckling simulations of the 15° configuration: 1st mode **(a)**, 2nd mode **(b)**, 3rd mode **(c)**, 4th mode **(d)**, 5th mode **(e)**, 6th mode **(f)**.

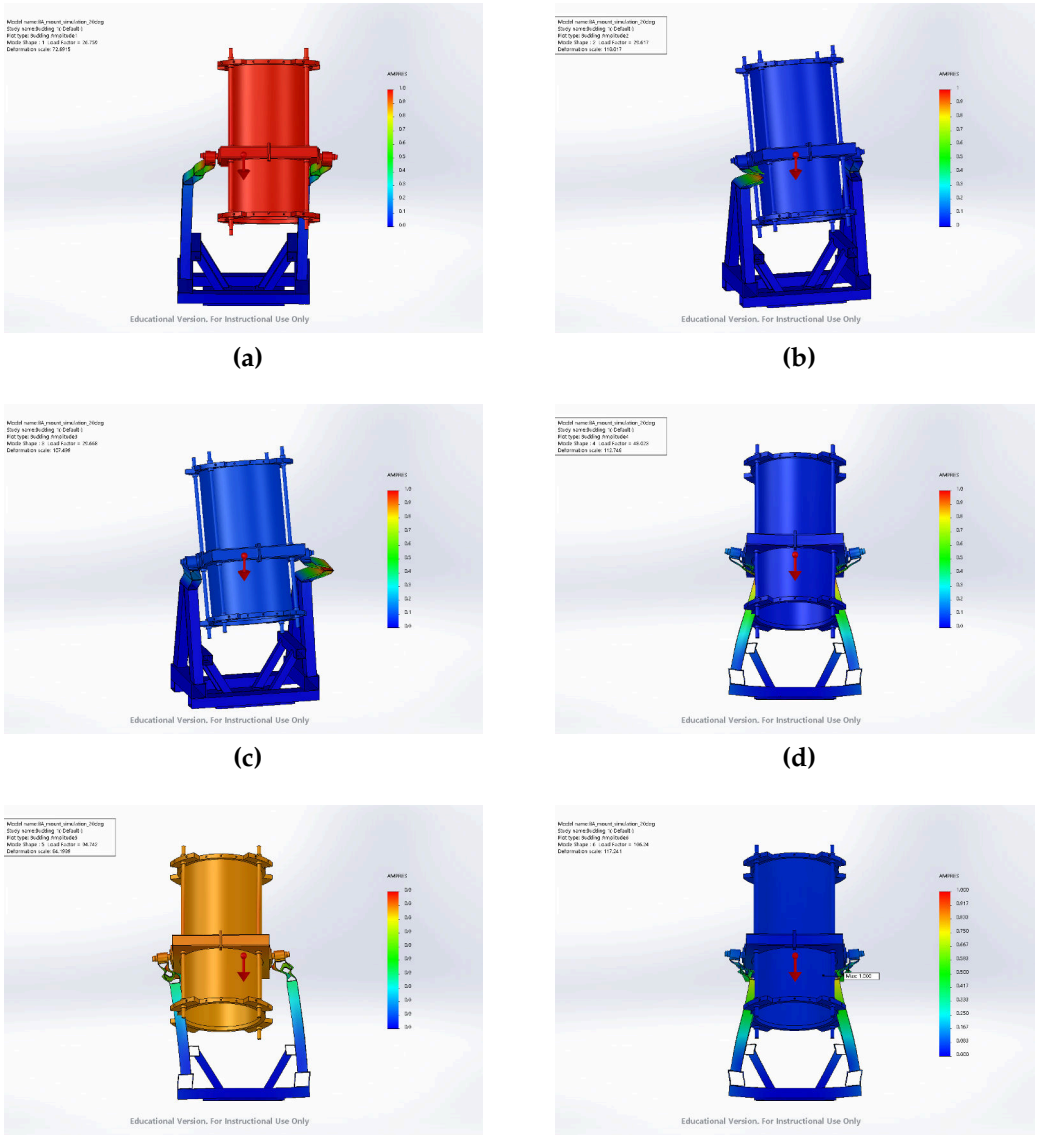

(a) **(b)**

(c) **(d)**

(e) **(f)**

Figure A.2.3: Buckling simulations of the 20° configuration: 1st mode **(a)**, 2nd mode **(b)**, 3rd mode **(c)**, 4th mode **(d)**, 5th mode **(e)**, 6th mode **(f)**.

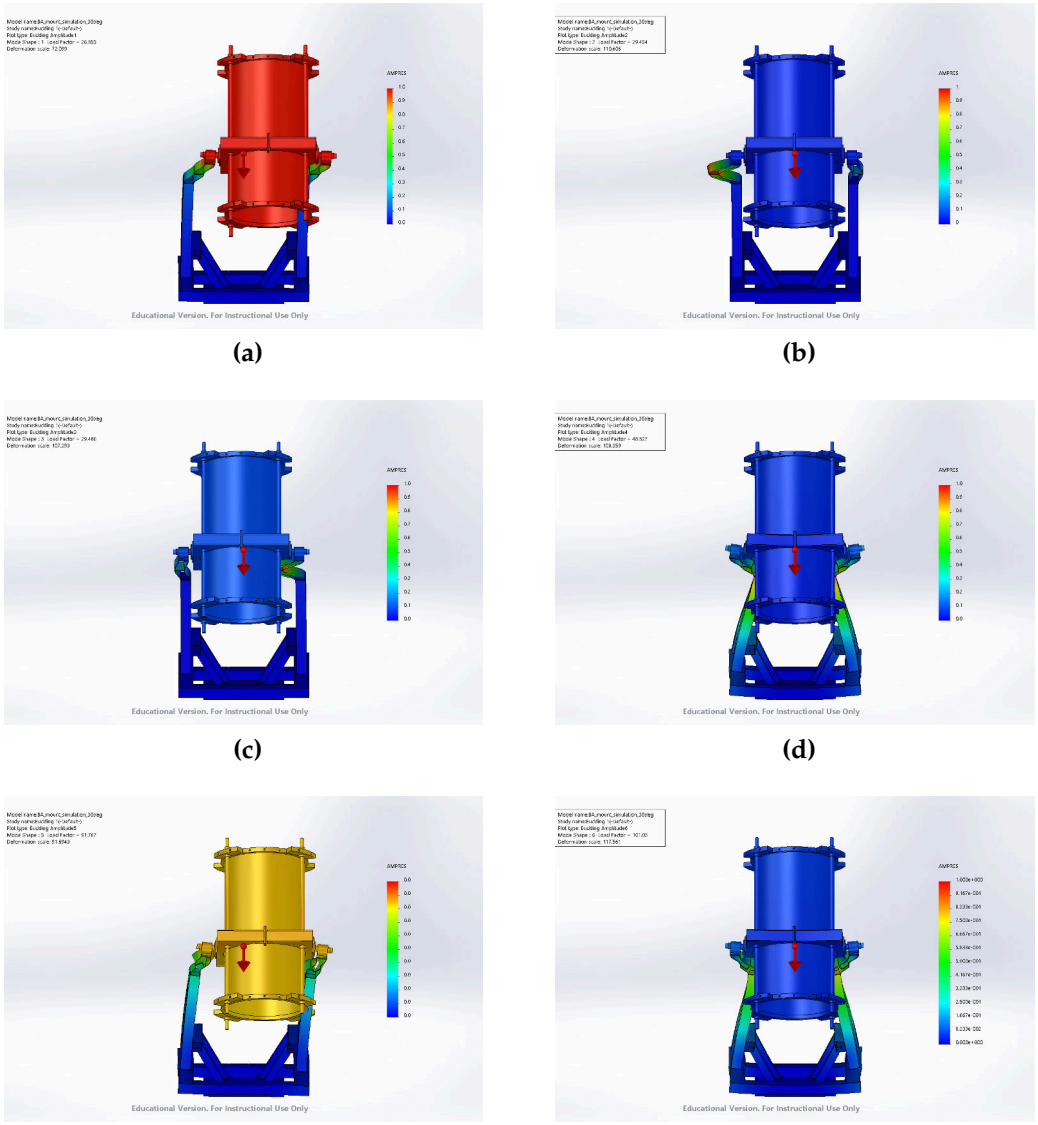

Figure A.2.4: Buckling simulations of the 30° configuration: 1st mode **(a)**, 2nd mode **(b)**, 3rd mode **(c)**, 4th mode **(d)**, 5th mode **(e)**, 6th mode **(f)**.

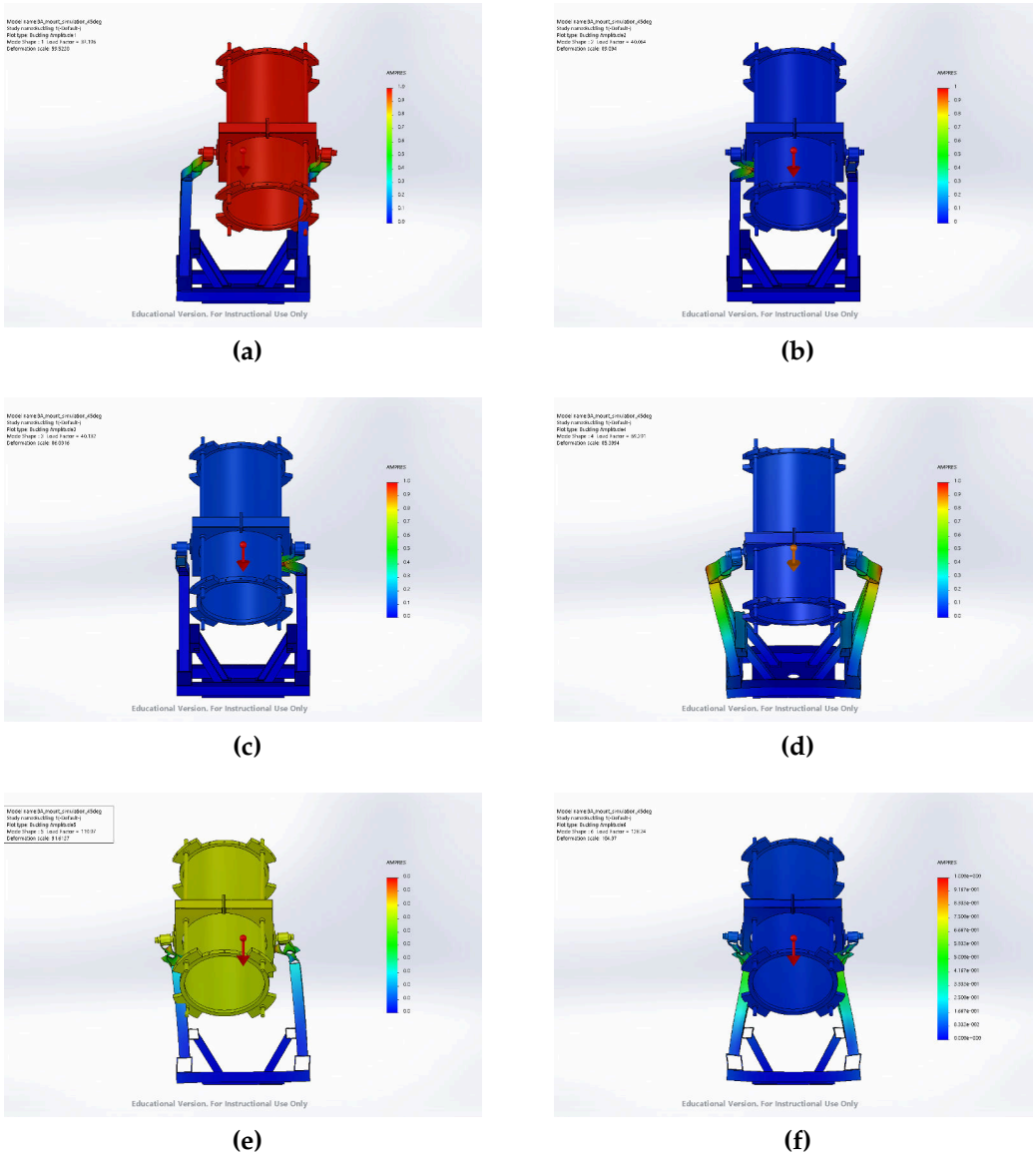

(a) **(b)** **(c)** **(d)** **(e)** **(f)**

Figure A.2.5: Buckling simulations of the 45° configuration: 1st mode **(a)**, 2nd mode **(b)**, 3rd mode **(c)**, 4th mode **(d)**, 5th mode **(e)**, 6th mode **(f)**.

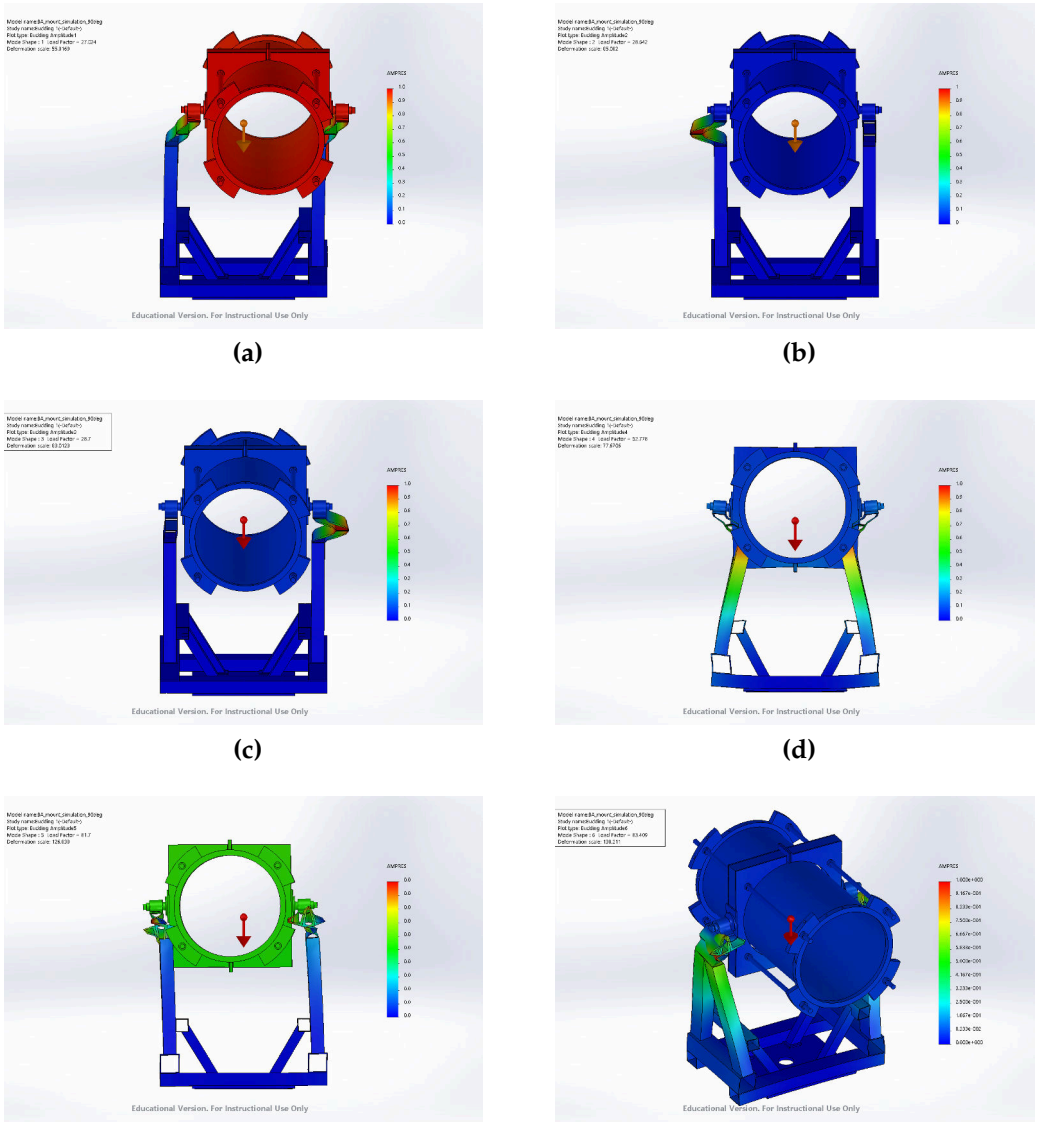

Figure A.2.6: Buckling simulations of the 90° configuration: 1st mode **(a)**, 2nd mode **(b)**, 3rd mode **(c)**, 4th mode **(d)**, 5th mode **(e)**, 6th mode **(f)**.

A.3 BASE

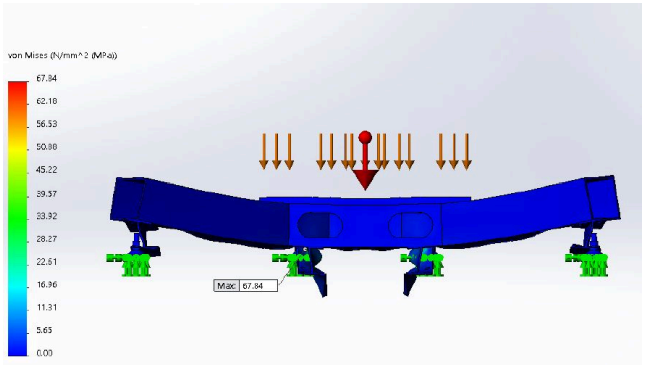

(a)

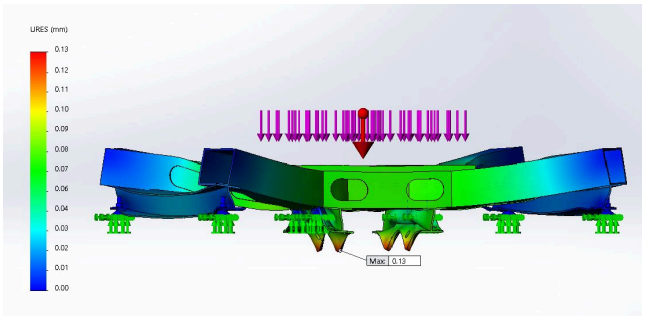

(b)

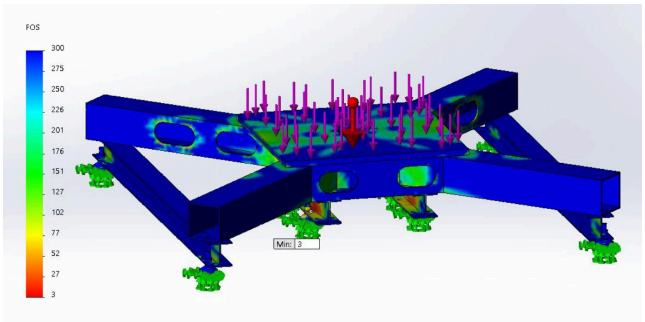

(c)

Figure A.3.1: Simulations of the v0 configuration: Von Mises stress **(a)**, displacement **(b)** and factor of safety **(c)**.

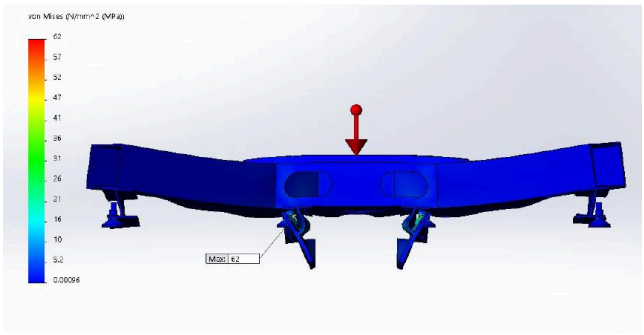

(a)

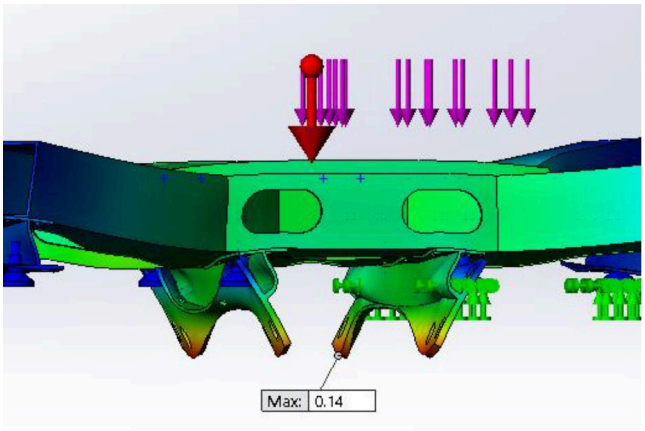

(b)

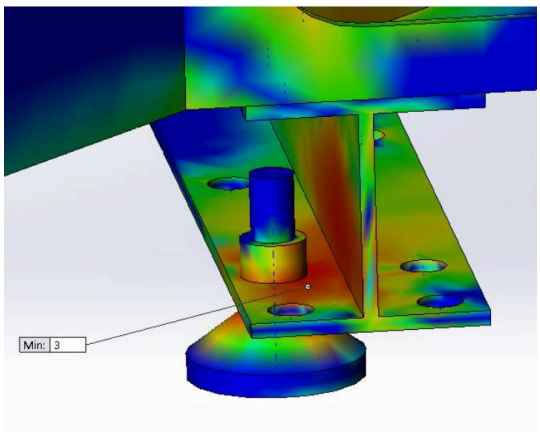

(c)

Figure A.3.2: Simulations of the v1 configuration: Von mises stress **(a)**, displacement (detail) **(b)** and factor of safety (detail) **(c)**.

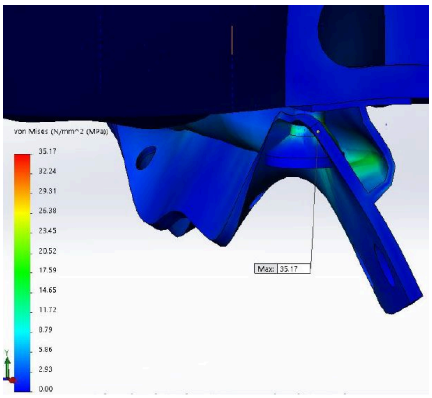

(a)

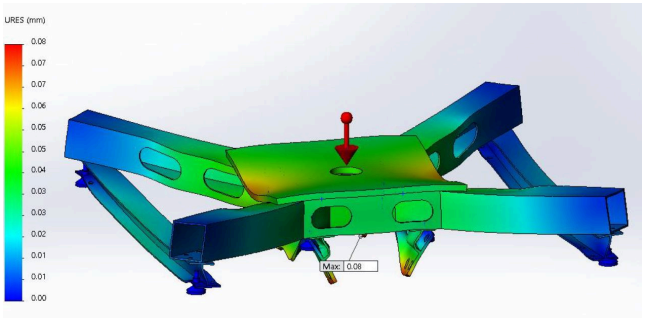

(b)

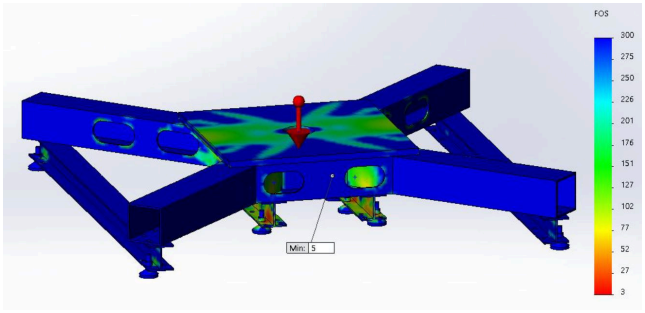

(c)

Figure A.3.3: Simulations of the v2 configuration: Von mises stress (detail) **(a)**, displacement **(b)** and factor of safety **(c)**.

B FEEDTHROUGH LEAK TEST

Before the first BICEP Array cryogenic run at Caltech a test was performed to investigate possible leaks from the connectors' flange (*feedthrough*) in order to assess if they were compatible with the pumping speed of the vacuum pump. The leak rate of the feedthrough was measured using a jig shown in Figure B.0.1 and a leak checker: before conducing the test both the leak detector and the jig were checked for leaks, both of them showing leaks $< 10^{-9} mbarls^{-1}$.

The test has been conducted on two different feedthrough plates, pumping on the jig and spraying ^{4}He on the connectors and on the side of the flanges. The measurements are summarized in Table B.0.1: the background values report the leak rate measured when not spraying, the leak rate values instead represent the peak value reached after spraying ^{4}He (in reality after this peak value was reached, the leak decreased to lower rates until returning to the background value).

The pump used with BICEP Array has a pumping speed (for ^{4}He) of $61 ls^{-1}$, while the nominal operational pressure to be achieved is $10^{-5} torr$.

	^{4}He Leak rate ($mbarls^{-1}$)	^{4}He Background ($mbarls^{-1}$)
Flange #1	2×10^{-8}	1.6×10^{-10}
Flange #2	7×10^{-7}	1.4×10^{-9}

Table B.0.1: Leak rate measurements for the two feedthrough flanges.

Figure B.0.1: The jig used for the feedthrough leak test; on the top side of the jig there is one of the flanges tested.

In presence of a leak q_L and pumping an effective speed (relative to the nature of a specific gas) S_{eff}, the ultimate pressure reached by the gas will be[1]:

$$p_{ult} = \frac{q_L}{S_{eff}}.$$

This value reflects the partial pressure due to ^{4}He, which needs to be corrected dividing by the molar fraction[2] of ^{4}He in air to obtain the ultimate air pressure inside the cryostat: the final results of this calculation are reported in Table B.0.2.

1 www.leyboldproducts.com/media/pdf/90/c7/87/Fundamentals_of_Leak_Detection_EN.pdf

2 The molar fraction of ^{4}He in dry air is 5.24×10^{-6}.

	Air ultimate pressure (mbar)	Air ultimate pressure (torr)
Flange #1	6.26×10^{-5}	4.69×10^{-5}
Flange #2	2.19×10^{-3}	1.64×10^{-3}

Table B.0.2: Expected ultimate pressures using the two feedthrough flanges.

From this calculation we chose to use the flange #1 for the first cryogenic run at Caltech: although it was expected that the ultimate pressure would have exceeded the nominal one by a factor of $\sim 4 - 5$, it has to be reminded that this calculation has been done using the *peak values* of the leak rate, hence overestimating the leak. This has been indeed confirmed as then the cryogenic run was performed without any leakage issue.

BIBLIOGRAPHY

[1] Crumrine, M., Ade, P. A. R., Ahmed, Z., Aikin, R. W., Alexander, K. D., Barkats, D., Benton, S. J., Bischoff, C. A., Bock, J. J., Bowens- Rubin, R., Brevik, J. A., Buder, I., Bullock, E., Buza, V., Connors, J., Cornelison, J., Crill, B. P., Dierickx, M., Duband, L., Dvorkin, C., Filippini, J. P., Fliescher, S., Grayson, J. A., Hall, G., Halpern, M., Harrison, S. A., Hildebrandt, S. R., Hilton, G. C., Hui, H., Irwin, K. D., Kang, J. H., Karkare, K. S., Karpel, E., Kaufman, J. P., Keating, B. G., Kefeli, S., Kernasovskiy, S. A., Kovac, J. M., Kuo, C. L., Larsen, N. A., Lau, K., Leitch, E. M., Lueker, M. V., Megerian, K. G., Moncelsi, L., Namikawa, T., Netterfield, C. B., Nguyen, H. T., O'Brient, R., Ogburn, R. W., Palladino, S., Pryke, C., Racine, B., Richter, S., Schwarz, R., Schillaci, A., Sheehy, C. D., Soliman, A., St. Germaine, T., Staniszewski, Z. K., Steinbach, B., Sudiwala, R. V., Teply, G. P., Thompson, K. L., Tolan, J. E., Tucker, C. E., Turner, A. D., Umiltà, C., Vieregg, A. G., Wandui, A., Weber, A. C., Wiebe, D. V., Willmert, J., Wong, C. L., Wu, W. L. K., Yang, E., Yoon, K. W., and Zhang, C. (2018). BICEP Array cryostat and mount design. In *Society of Photo-Optical Instrumentation Engineers (SPIE) Conference Series*, volume 10708, page 107082D.

[2] Guth, A. H. (1981). Inflationary universe: A possible solution to the horizon and flatness problems. , 23:347–356.

[3] Hui, H., Ade, P. A. R., Ahmed, Z., Aikin, R. W., Alexander, K. D., Barkats, D., Benton, S. J., Bischoff, C. A., Bock, J. J., Bowens-Rubin, R., Brevik, J. A., Buder, I., Bullock, E., Buza, V., Connors, J., Cornelison, J., Crill, B. P., Crumrine, M., Dierickx, M., Duband, L., Dvorkin, C., Filippini, J. P., Fliescher, S., Grayson, J., Hall, G., Halpern, M., Harrison, S.,

Hildebrandt, S. R., Hilton, G. C., Irwin, K. D., Kang, J., Karkare, K. S., Karpel, E., Kaufman, J. P., Keating, B. G., Kefeli, S., Kernasovskiy, S. A., Kovac, J. M., Kuo, C. L., Lau, K., Larsen, N. A., Leitch, E. M., Lueker, M., Megerian, K. G., Moncelsi, L., Namikawa, T., Netterfield, C. B., Nguyen, H. T., O'Brient, R., Ogburn, R. W., Palladino, S., Pryke, C., Racine, B., Richter, S., Schwarz, R., Schillaci, A., Sheehy, C. D., Soliman, A., St. Germaine, T., Staniszewski, Z. K., Steinbach, B., Sudiwala, R. V., Teply, G. P., Thompson, K. L., Tolan, J. E., Tucker, C., Turner, A. D., Umiltà, C., Vieregg, A. G., Wandui, A., Weber, A. C., Wiebe, D. V., Willmert, J., Wong, C. L., Wu, W. L. K., Yang, E., Yoon, K. W., and Zhang, C. (2018). BICEP Array: a multi-frequency degree-scale CMB polarimeter. In *Society of Photo-Optical Instrumentation Engineers (SPIE) Conference Series*, volume 10708, page 1070807.

[4] Kamionkowski, M. and Kovetz, E. D. (2016). The Quest for B Modes from Inflationary Gravitational Waves. *Annual Review of Astronomy and Astrophysics*, 54:227–269.